arXiv:astro-ph/9812152v1 8 Dec 1998

A recalibration of *IUE* NEWSIPS low dispersion data

D. Massa

Raytheon STX, NASA/GSFC, Mailstop 631.0, Greenbelt, MD 20771; massa@xfiles.gsfc.nasa.gov

and

E. L. Fitzpatrick

Astronomy Department, Villanova, Villanova, PA 19085; fitz@ast.vill.edu

ABSTRACT

While the low dispersion *IUE* NEWSIPS data products represent a significant improvement over original *IUE* SIPS data, they still contain serious systematic effects which compromise their utility for certain applications. We show that NEWSIPS low resolution data are internally consistent to only 10-15% at best, with the majority of the problem due to time dependent systematic effects. In addition, the NEWSIPS flux calibration is shown to be inconsistent by nearly 10%.

We examine the origin of these problems and proceed to formulate and apply algorithms to correct them to $\sim 3\%$ level – a factor of 5 improvement in accuracy. Because of the temporal systematics, transforming the corrected data to the *IUE* flux calibration becomes ambiguous. Therefore, we elect to transform the corrected data onto the *HST* FOS system. This system is far more self-consistent, and transforming the *IUE* data to it places data from both telescopes on a single system.

Finally, we argue that much of the remaining 3% systematic effects in the corrected data is traceable to problems with the NEWSIPS intensity transformation function (ITF). The accuracy could probably be doubled by rederiving the ITF.

Subject headings: instrumentation: spectrographs — methods: data analysis — techniques: photometric — ultraviolet: general

1. Introduction

This paper addresses problems with the absolute flux calibrations, thermal corrections, and time-dependent sensitivity corrections of the *IUE* (Boggess et al. 1978) low-dispersion NEWSIPS ("final archive") data (Nichols & Linsky 1996, NL hereafter). We demonstrate that there are systematic errors of up to 15 % in NEWSIPS fluxes and describe correction procedures which reduce the systematics to a level compatible with the best possible signal-to-noise ratio achievable by a single *IUE* spectrum, i.e, $\sim 3\%$.

While carrying out an independent research program which involved fitting Kurucz (1991) model atmospheres to NEWSIPS low-dispersion data of B-type stars (Fitzpatrick & Massa 1999), it became apparent that the absolute flux calibration was suspect. The basis of our suspicion was that the model fit residuals were large, strongly wavelength dependent, *and independent of stellar spectral type*. Since we were fitting energy distributions of main sequence stars throughout the range $10,000 < T_{eff} < 30,000$ K, it was difficult to imagine a single ionic signature that would produce such an effect. Consequently, we performed a detailed assessment of the NEWSIPS low-dispersion data, ultimately involving more than 4600 spectra. This investigation revealed that not only is the absolute flux calibration of the NEWSIPS data inconsistent with its proposed standard, but that the data also contain serious thermal and time-dependent systematics.

The nature of the NEWSIPS absolute flux calibration problem is illustrated in Figure 1, which compares the available *IUE* NEWSIPS SWP and LWP data (see §3), *HST* FOS data, and models for the hot white dwarf G191B2B. The top spectrum is a ratio of the *IUE* NEWSIPS data and the Finley & Koester (FK) model used to define the *IUE* calibration (NL). There is obvious disagreement between the model and the NEWSIPS data, averaging $\sim 5\%$ and as large as 10% in the LWP. Furthermore, the wavelength-dependent structure in the ratio is nearly identical to the T_{eff}-independent residuals we observed in our B star fits — including the high frequency "noise" visible in the figure — indicating that this results from systematic calibration errors and *not* from random noise. The middle plot is the ratio of the FOS fluxes of G191B2B divided by the model provided by Koester to calibrate the FOS (Bohlin 1996, B96 hereafter). In this case, the agreement is excellent, but not exact, since G191B2B was only one of 8 white dwarfs used to calibrate the FOS (B96). The bottom plot is a ratio of the NEWSIPS and FOS data. It is very similar to the top ratio, but is also displaced downward by a wavelength independent, gray, displacement of $\sim$ 2-3%. The displacement results from the *IUE* and FOS projects adopting slightly different models and different scalings for their UV calibrations; FOS is based on optical photometry calibrations (B96), and *IUE* on UV calibrations (NL).

An example of the systematic time-dependent effects present in NEWSIPS data is illustrated in Figure 2 for the *IUE* LWR camera. This plot shows the mean LWR flux in the wavelength band $2400 < \lambda < 2800$ Å for 3 standard stars as a function of time during the years when the LWR was the default long wavelength camera. The data for each star were normalized by the overall mean for that star during the entire time interval. Notice that each star shows the same time-dependence, indicating that the effect is instrumental, and not intrinsic to a particular object. The magnitude of the effect over this period is roughly 10%. The LWR camera shows the largest level of time-dependence. A preliminary discussion of the time dependent behavior of both the NEWSIPS low *and* high dispersion data can be found in Massa et al. (1998).

High frequency ("noise-like") temporal systematics are also present in the data. Figure 3 illustrates these effects. We first normalize the large aperture spectra of 3 *IUE* standard stars (HD 60753, BD+28°4211 and BD+75°375 – see §3) by their mean spectra. The normalized spectra were then arranged chronologically. The first 40 spectra of this set were divided into 2 20–spectrum samples – each composed of every other spectrum. This insures that the 20–spectrum samples have effectively identical temporal distributions, so time dependent systematics affect their means in the same way. The top curve in each panel is a ratio of the 2 20–spectrum means. The middle curve in each panel is a ratio of 2 20–spectrum means obtained from the last 40 spectra of the same 3 star sample and similarly prepared. Finally, the bottom plot in each panel is a ratio of the 2 40–spectrum means obtained from all of the spectra used in the first and second curves. While time dependent effects will cancel in the first 2 curves, they are maximized in the last one, since it compares data obtained at the beginning and end of the mission. If the high frequency structure was due to random noise, its amplitude in the bottom

curve would be $1/\sqrt{2}$ times smaller than in the top two curves, since twice as many spectra are used to produce the ratio. However, the amplitude of the high frequency structure is clearly larger in the bottom ratio! This is because much of the structure is not due to random noise, but to time dependent effects in the data. Figure 3 demonstrates that the peak-to-peak amplitude of the high frequency systematics often exceeds 10%.

In addition to temporal effects, residual temperature effects are also present in the NEWSIPS data. These are characterized by the camera head amplifier temperature, *THDA*, measured at the beginning of the exposure (these values are supplied as part of the NEWSIPS headers, see, Garhart et al., 1997). The *THDA* effects are localized in wavelength. To demonstrate the effect, we used the same data set described in the previous paragraph, and binned them over a small wavelength band. These data are then plotted in chronological order in the top portions of Figures 4a and b. The same data are then rearranged by *THDA* value and plotted in the lower portions of the figures. The presence of a systematic *THDA* effect on the order of 5% is obvious. We only show the LWP and SWP data, since the large temporal effects in the LWR data tend to obscure the smaller *THDA* systematics.

The previous examples demonstrate that the *IUE* absolute flux calibration is inconsistent with its reference model by as much as 10%, that the LWR data contain time-dependent errors of similar magnitudes, that all of the data contain high frequency temporal effects whose amplitudes exceed 10%, and that thermally induced systematics on the order of 5% are also present. We emphasize that systematic errors of this order can be important in many applications and must be corrected for the following reasons:

1. To utilize the unprecedented temporal baseline of *IUE*, time dependent instrumental drifts in the data must be corrected to the level of the maximum achievable S/N.

2. To take full advantage of the signal-to-noise (S/N) capabilities of *IUE*, an absolute calibration whose uncertainty is equal to or less than the maximum achievable S/N is required.

3. Time dependent dependent high frequency structure can mimic the strengthening or weakening of spectral features. These effects can produce misleading interpretations and act to nullify potential noise reductions gained by averaging spectra. They must be reduced to the level of typical point-to-point noise.

So what is the maximum achievable S/N for *IUE* data? In spite of the limited dynamic range of the *IUE* detectors, we demonstrate in §3 that a $S/N \sim 30:1$ should, in principle, be possible for a single spectral resolution element in an optimally exposed spectrum. Furthermore, many bright objects were either observed more than once or else observed in the trail mode, which could increase the S/N by a factor 2 (see §3). As a result, a large fraction of the objects in the *IUE* archive have a potential $S/N \sim 30:1$ – roughly 4 - 5 times more accurate than the current NEWSIPS calibrations.

In the following sections we examine more closely the systematic effects present in *IUE* NEWSIPS data and present a scheme for the removal of these effects and a correction to the absolute calibration. Bless and Percival (1998) performed a critical review of the available UV calibrations and deduced that the FOS absolute calibration is superior. Consequently, we elected to derive a transformation between the *IUE* NEWSIPS and FOS systems, rather than recalibrating *IUE* using the G191B2B model. This also insures that both datasets are on a common scale.

In §2, we introduce the stars to be used in our analysis and indicate which ones will be used to determine temporal and thermal trends, to derive an absolute flux calibration, and to verify the results. In §3, we describe some basic characteristics of *IUE* and explain the different observing modes and why each must be calibrated separately. We also discuss how the available data were culled into our final sample. In §4, we describe the mathematical formulation of how we correct for systematic effects. In §5 we apply the analysis to the *IUE* data and present our results. In §6, we verify our results by applying them to sequences of spectra not included in the derivation of the corrections. In §7, we analyze both the random and systematic errors present in the corrected data. In §8, we summarize our conclusions and discuss the availability of IDL programs which apply the corrections to NEWSIPS low dispersion data.

2. The program stars

Basic data for the program stars used in this study are listed in Table 1. The stars were selected from the

IUE standard stars compiled by Pérez et al. (1990) and from the FOS calibration stars given in B96. We also indicate in the table the role of each star in our analysis. The "temporal/thermal standards" are used derive the time- and temperature- dependence of the instrumental response, and the "temporal/thermal control" stars are used to verify the results. The "flux standards" are the stars used to derive the transformation between the *IUE* NEWSIPS and FOS flux scales and the "flux control" stars are used to verify these results.

3. The data

In this section, we describe the selection of the spectra used in our analysis. We begin with a discussion of a few general characteristics of *IUE* data and observations (§3.1) and then describe the 4 *IUE* observing modes (§3.2). Lastly, we list the criteria used to select or reject individual spectra and individual data points (§3.3). For a more detailed description of the general properties of *IUE* and its data, see Newmark et al. (1992) and Garhart et al. (1997).

3.1. Overview

IUE had two UV spectrographs, covering the short and long wavelengths regions. Each spectrograph could send its output to either of 2 (primary and redundant) cameras. Consequently, *IUE* spectra are referred to as long wavelength primary (LWP), long wavelength redundant (LWR) or short wavelength prime (SWP). The short wavelength redundant camera never operated properly and there are no NEWSIPS data for it. The wavelength coverages of the spectrograph/camera combinations were $1150 < \lambda < 1975$ Å for the SWP, $1910 < \lambda < 3300$ Å for the LWP and $1860 < \lambda < 3300$ Å for the LWR.

Each spectrograph could be accessed through one of 2 object apertures. One was a 10×20 arc sec oval, the large aperture, and the other was a 3 arc sec circle, the small aperture. The size of the telescope image in the aperture plane was ~ 4 arc sec at best, and thus overfilled the small aperture by a large margin (see Garhart et al. for a more detailed discussion).

The *IUE* detectors had 768×768 pixels and each pixel had a very limited dynamic range, with only 256 distinct output levels (8 bits). Since *IUE* was in high earth orbit, part of the output signal was due to particle background, as well as to a pedestal of read noise. Consequently, the maximum S/N possible for a single pixel was $\sim 10:1$ (see Ayers 1993 for a more thorough discussion). Since a low dispersion spectrum typically had a full width perpendicular to the dispersion of about 3 pixels, the maximum S/N of a *spectral pixel* was $\sim \sqrt{3} \times 10$ or $\simeq 17:1$. Furthermore, ~ 3 spectral pixels make up a *spectral resolution element*, so the maximum S/N for a *single spectral element* was $\sim \sqrt{3} \times \sqrt{3} \times 10$, or $\simeq 30:1$. However, such high S/N rarely occurred over a large spectral range since the limited dynamic range of the detector made it necessary to under expose some pixels in order to avoid saturating others. Nevertheless, when multiple exposures of the same object are averaged, a $S/N \sim 30:1$ should be attainable over broad spectral regions. Therefore, our goal is to reduce the systematic effects in the *IUE* data to a similar level, i.e., $\sim 3\%$.

Once an exposure was obtained, the *IUE* cameras had to be read and then prepared for the next exposure. This "read-prep" operation typically required about 20 minutes. This was often far longer than the actual exposure times and several of the observing strategies described below were intended to minimize the impact of the read-prep overhead time.

Finally, the *IUE* satellite locked onto its target using its Fine Error Sensor (FES). In this mode, the satellite could point to a fixed position on the sky with an accuracy of 0.25 arc sec.

3.2. The observing modes

IUE spectra were obtained in one of 4 observing modes, each of which had its own unique advantages. These 4 observing modes were:

Large Aperture: This mode simply involved obtaining spectra by centering the object in the large aperture and was the primary observing mode. Since the large aperture was ~ 3 times larger than the image of a point source produced by the *IUE* optics, the 0.25" tracking capability of *IUE* was not critical for large aperture exposures, and the photometric quality of these data is the best.

Small Aperture: In this mode, the star was centered in the small aperture. Since the image was considerably larger than the aperture, the exact amount of flux entering the detector was highly dependent upon the pointing. Consequently, the overall photometric quality of these data is very poor, varying by as much as a factor of two. Nevertheless, small aperture could be valuable for several reasons. First,

low dispersion large and small aperture spectra were well-separated on the detector and so both could be recorded without an intervening read-prep. Thus the overhead requirements and poor dynamic range of the detectors could be circumvented to some degree by exposing the large and small aperture spectra to different signal levels and later combining the extracted data. (Small aperture data would be scaled to the photometric level defined by large aperture using data in mutually well-exposed wavelength regions.) Second, small aperture spectra had slightly better spectral resolution, due to the smaller image on the detector. Third, sometimes it was necessary to use the small aperture in order to isolate objects in crowded fields.

Trailed: In this mode, the star was allowed to drift across the large aperture, in the cross-dispersion direction, during an exposure. This produced a widened spectrum which had 2 advantages. First, since nearly 4 times as many pixels were exposed, trailed spectra have nearly twice the S/N of large aperture spectra with the same read-prep time. Second, since more pixels contribute to a single resolution element, trailed spectra are less sensitive to localized detector irregularities (fixed pattern noise). On the other hand, the photometric accuracy of trailed spectra is somewhat inferior to that of large aperture spectra because the exposure time depends on the exact trajectory of the object through the aperture and the exact drift rate. Further, during the maneuver, the spacecraft had to rely on its gyros for stability and could not take advantage of the FES feedback. As a result of these effects, trailed spectra typically have the best relative photometric accuracy, but their overall flux level is slightly less accurate than large aperture spectra.

Multiple exposures: In this mode, the star was placed at 2 or 3 distinct locations perpendicular to the dispersion in the large aperture. The net result is a widened spectrum, although it is not uniformly exposed (hence, this mode was often referred to as the pseudo-trail mode). Since FES tracking was in effect throughout the exposures, the photometric accuracy of these spectra are probably better than for trailed spectra, but the standard stars were not observed often enough in this mode to verify this supposition.

For the purposes of this paper, 2 important points emerge from the preceding discussion.

1. Each observing mode exposed different portions of the detector. Therefore, the temporal and thermal behavior and absolute calibration of each mode must be considered separately. Unfortunately, we lack the data to do this for the pseudo-trail mode and it will have to be calibrated from the other modes.

2. Errors in *IUE* spectra typically contain two distinct components: *point-to-point* (or relative) errors which are important for measuring spectral features, and *scaling errors*, which affect the overall level of the spectra and are important in fitting models or in concatenating *IUE* spectra with each other or with optical photometry. The relative magnitude of these 2 types of error depends upon the observing mode. Furthermore, the scaling errors (which originate from pointing and focus inaccuracies) can sometimes be quite large.

There are additional effects which can have a strong influence on *IUE* spectra. For instance, the particle background rate could sometimes become rather large, reducing the S/N of spectra of even bright objects to only a few. There were also non-random effects which included microphonics noise (referred to as "PINGS") and minor frame telemetry drop outs, which typically have a strong affect on a localized portion of the spectrum. See Garhart et al. (1997) for a more complete discussion of these and other effects.

3.3. Data selection

Table 2 contains information on the *IUE* NEWSIPS data used for this analysis. We submitted a request to the NSSDC for all of the available NEWSIPS low resolution spectra for the stars listed in Table 1 at the end of 1998 March. All but a few spectra were available at that time. The delivered data were then screened as follows:

1. The ranges of exposure times were restricted depending on the object, camera, observing mode, and application. In Table 2, t_{min} and t_{max} give the lower and upper limits, respectively, on acceptable exposure times.

2. The LWR sample was restricted to the time period when the LWR was the default long wavelength camera (1978 – 1984).

3. Outliers were rejected. These were defined as follows: The mean flux for each spectrum was determined over a pre-specified wavelength interval ($1400 - 1700$ Å for the SWP and $2400 - 2800$ Å for the LWR and LWP). The sample mean and RMS scatter (σ) were determined for these mean fluxes. If the absolute value of the difference between the mean flux for a given spectrum and the sample mean differed by more than 3σ, then the spectrum was rejected. This criterion was applied iteratively until no additional spectra were rejected.

4. A few LWRs were rejected "by hand" because, although they passed the outliers criteria, their shapes were distinctly peculiar. All of these were observations of HD 60753 and most of them were affected by "pings" (data drop outs) or extreme background levels.

The number of spectra which survived the screening process outlined above is listed in the last column of Table 2 for each star and observing mode. Within each acceptable spectrum, data points with ν-Flag values (see Garhart et al. 1997) equal to 0 (no known problem), -128 (on the positively extrapolated ITF) or -256 (on the negatively extrapolated ITF) were given weights of unity and all other points were assigned zero weight.

Finally, we note that there are two distinct ITFs for LWR spectra (see Garhart et al. 1997) and these result in slightly different wavelength scales. Further, ITF A (identified as LWR83R94 in the MXLO headers) results in spectra with 563 data points while ITF B (LWR83R96 in the headers) spectra have 562 points. We used the wavelength scale from ITF A for all of the LWR spectra. This ignores a difference between the 2 wavelength scales which increases linearly from 0.2 Å at 1950 Å to 1.66 Å at 3150 Å (the longest wavelength we calibrate). However, since even the largest deviation is smaller than the sampling interval (2.67 Å) and much smaller than a resolution element ($\sim$ 7 Å at the longer wavelengths), we felt that interpolating the data from one grid to the other was unwarranted. Therefore, we simply accept the minor systematic error which arises from adopting a common wavelength scale for all of the spectra.

4. Mathematical description of the analysis

To bring the NEWSIPS data onto a common scale with the FOS data, we must first remove its time and *THDA* dependencies. We do this by fitting the dependencies and then applying the results to correct the data for the systematics. We then derive the transformation between the corrected data and the FOS system. In this section we provide a mathematical outline of the problem. We describe its application to the data in §5.

4.1. The corrections

We wish to analyze $\{i = 1, \ldots, M\}$ standard stars observed at different wavelengths and times to determine the time degradation and *THDA* dependence of the instrumental response. In the analysis, we adopt the following model of the temporal, t, and *THDA*, T, dependence for the i^{th} standard:

$$f(\lambda, t, T)_i = f(\lambda, t_0, T_0)_i g(\lambda, t - t_0) h(\lambda, T - T_0) \quad (1)$$

where $g(\lambda, t - t_0)$ and $h(\lambda, T, T_0)$ are assumed to be universal multiplicative functions which describe the time and *THDA* dependencies of the instrumental response at λ and are equal to 1 at $(t, T) = (t_0, T_0)$. The fact that we have written the t and T dependencies as separate functions implicitly assumes that the *form* of the *THDA* dependence does not change with time and that the temporal dependence is the same for all values of *THDA*.

Taking logarithms linearizes the problem, *viz.*,

$$\log f(\lambda, t, T)_i = \log f(\lambda, t_0, T_0)_i + \log g(\lambda, t - t_0) + \log h(T - T_0) \quad (2)$$

A simple form for the functions $\log g(\lambda, t - t_0)$ and $\log h(\lambda, T - T_0)$ which satisfy our assumptions is

$$\log g(\lambda, t - t_0) = \sum_{k=1}^{K} a(\lambda)_k (t - t_0)^k \quad (3)$$

$$\log h(\lambda, T - T_0) = \sum_{l=1}^{L} b(\lambda)_k (T - T_0)^l \quad (4)$$

i.e., K and L^{th} order polynomials.

It is possible to fit the data set for each standard star individually using the previous equation,

thereby obtaining the two sets of coefficients, $\{a(\lambda)_k\}$ and $\{b(\lambda)_l\}$, and the flux at the fiducial values, $\log f(\lambda, t_0)_i$, for each standard star separately. However, we would like to fit the data of the M standards *simultaneously*, thereby determining a universal estimate of the coefficients, utilizing all of the available data. To accomplish this, we first concatenate the data into a single data set. If there are $\{m = 1, \ldots, M\}$ standard stars, each with N_m observations at times $\{t_n | n = 1, \cdots, N_m\}$, at each wavelength λ, then the concatenated series $\{y(\lambda, t)\}$ is defined as,

$$\begin{aligned}\{y(\lambda,t,T)\} \equiv \quad & \{\log f(\lambda,t_1)_1, \ldots, \log f(\lambda,t_{N_1})_1, \\ & \log f(\lambda,t_1)_2, \ldots, \log f(\lambda,t_{N_2})_2, \\ & \ldots, \log f(\lambda,t_1)_K, \ldots, \\ & \log f(\lambda,t_{N_M})_M\} \end{aligned} \quad (5)$$

The temporal and *THDA* dependence of the combined data set at each wavelength is then fit with a standard linear regression model of the form

$$\begin{aligned} y(\lambda,t,T) = \quad & \textstyle\sum_{m=1}^{M} \log f(\lambda,t_0)_m \mathbf{X}_{0m} + \\ & \textstyle\sum_{k=1}^{K} a(\lambda)_k \mathbf{X}_k + \sum_{l=1}^{L} b(\lambda)_l \mathbf{Y}_l \end{aligned} \quad (6)$$

where the $\mathbf{X}_{0m}$ are "box-car" functions which are either 0 or 1, depending on whether the data refer to the m^{th} star, the $\mathbf{X}_k$ are polynomials of the form $(t - t_0)^k$, and the $\mathbf{Y}_k$ are polynomials of the form $(T - T_0)^k$, where the t and T are the time and *THDA* corresponding to the particular term.

As pointed out in §3, the major source of error in the spectra is often an overall scaling factor due to inexact centering of the object in the aperture or slight trailing errors. To suppress this effect, we normalized the spectra by their mean flux over a wavelength band $\lambda_1 < \lambda < \lambda_2$. These normalized spectra are denoted as $r(\lambda, t, T)$. The $r(\lambda, t, T)$ are fit at each wavelength by equation 6, and then the normalization constants are fit independently the same way. As a result, we determine 3 sets of coefficients, the $\{a(\lambda)_k\}$ and $\{b(\lambda)_l\}$ in equation 6 (except now they apply to the $r(\lambda, t, T)$) and a set $\{a_{0k}; b_{0l}\}$, which fit the level of the flux in the standard band, relative to its value at $t = t_0$, $T = T_0$. Consequently, to correct the flux of an object observed at time t with $THDA = T$, one must divide the observed flux by the function:

$$\begin{aligned} g(\lambda, t - t_0) h(\lambda, -T_0) = \quad & \prod_{k=1}^{K} 10^{[a(\lambda)_k + a_{0k}](t-t_0)^k} \times \\ & \prod_{l=1}^{L} 10^{[b(\lambda)_l + b_{0l}](T-T_0)^l} \end{aligned} \quad (7)$$

The result is how the spectrum would have appeared if it had been obtained at $t = t_0$ with $THDA = T_0$.

Finally, since there are not enough pseudo-trail spectra to perform an independent calibration, this case is treated differently, and discussed in §5.3.

4.2. Flux scale transformation

Once the temporal and thermal corrections are determined, the transformation to the FOS flux scale is relatively straightforward. It is simply a mean of the ratios of the FOS spectra of the "flux standards" (rebinned to *IUE* resolution) to their mean *IUE* spectra.

5. Application of the analysis

In this section we provide the details of the general analysis outlined in the previous section, as applied to the data for the program stars listed in Table 1.

5.1. Temporal and *THDA* corrections

In performing the fits, we used sixth degree polynomials in both t and T for the $g(\lambda, t)$ and $h(\lambda, T)$. The time, t, was expressed in Julian years, and $t_0 = 2445000/365.25$ (1 Feb. 1 1982). The fiducial *THDA* value, T_0, was set to 9 for the SWP and LWP data and 13 for the LWR. Due to a paucity of data at extreme *THDA* values, *THDA*s of SWP and LWP data less than $T_{min} = 6$ were set equal to 6 and values greater than $T_{max} = 13$ were set equal to 13. The same process was used for the LWR data except with $T_{min} = 11$ and $T_{max} = 16$.

For normalizing the spectra to obtain $r(\lambda, t, T)$, we used 150 data points in the range $2399.69 < \lambda < 2796.43$ Å for the LWP and LWR and 179 points in the range $1400.35 < \lambda < 1698.74$ Å for the SWP.

The stars HD 60753, BD+28°4211 and BD+75°375 were used as primary standards for the corrections because they have the largest number of spectra, and these span the entire lifetime of *IUE*. BD+33°2642 and HD 93521 have the next largest number of spectra (roughly half of any one of the primary standards), and excellent temporal coverage. These objects will

be used to verify the results derived from the 3 standards (see §6).

Figures 5a-c give examples of the fits to the time trends in the relative scale factors and at the specific wavelengths for the 3 *IUE* cameras. The solid curves are the fits for $THDA = T_0$, and the dashed curves are for the cases $T - T_0 = 0.75(T_{max} - T_0)$ and $T - T_0 = 0.75(T_{min} - T_0)$. The fits for the extreme *THDA* values usually parallel the $T = T_0$ curve and typically represent a much smaller effect (as expected from our discussion in §1). Data from the 3 standards used to determine the fits are depicted by different symbols. Each of the individual wavelength plots shown are actually the means of 3 adjoining wavelength points, to reduce the overall noise. It is clear that the data for the 3 stars are completely interspersed and that the solution is consistent with all three. Several other aspects of the plots are of interest.

1. There are no major time systematics in the LWP data (Fig. 5a).
2. Data longward of 3100 Å become very unreliable in both of the long wavelength cameras (Figs. 5a-b).
3. The signal-to-noise of data shortward of 2000 Å is very poor in the LWP data, but relatively good in the LWR (Figs. 5a-b).
4. The large time dependent systematic in the scaling of the LWR data is clearly demonstrated (Fig. 5b).
5. All but the shortest wavelengths of the SWP data have comparable signal-to-noise (Fig. 5c).
6. Strong systematic effects are present in the short wavelength SWP data (Fig. 5c).
7. The SWP data are generally of higher quality (recall that these are all comparable exposures). Both the scale factors and the individual wavelength fits have smaller dispersions in the SWP data.

5.2. Flux transformations

Once the spectra are corrected to their fiducial time and *THDA* values, the transformation to the FOS system is straightforward. The stars used to determine the flux transformation were BD+28°4211, BD+75°375, BD+33°2642 and G191B2B. Both FOS and high quality *IUE* data are available for each of these. HD 60753 was not observed with FOS, but will provide a powerful verification of the flux calibration.

The FOS data were first smoothed to the *IUE* resolution using the data provided by Garhart et al. (1997). These spectra were then sampled onto the *IUE* grid. There is, however, one complication. In order to make the sharp He I features located throughout the long wavelength *IUE* spectra of BD+75°375 cancel with their counterparts in the FOS spectra, it was necessary to adjust the wavelength scale of the long wavelength cameras. Since experience has given us considerably more confidence in the FOS calibrations, we adopted the FOS wavelength scale and derived a set of adjustments for the *IUE* scale. The measured differences are listed in Table 3. In practice, we applied a spline interpolation between these points.

Figures 6a-c show the ratios of the completely corrected large aperture data (with the wavelength corrections applied to the long wavelength data) divided by the corresponding FOS data. Curves from the 4 primary standards, BD+28°4211, BD+75°375, BD+33°2642 and G191B2B are depicted by different line styles. The mean curve, used for the calibration, was formed by first adjusting all of the ratios to the sample mean value across the same wavelength bands described above and then determining a weighted mean ratio, where the weighting factors were just the number of observations that entered each ratio. The standard deviation of the weighted mean ratio was also calculated and is shown at the bottom of each plot. The excellent agreement of the different curves emphasizes the reality of the structure, including the large point-to-point structure. The RMS dispersion shows that the overall internal agreement of the calibration curves is $\sim 1\%$ – well within our goal. The trailed and small aperture ratios have similar scatters. It is interesting that the feature referred to as the 1515 Å feature by Garhart et al. (1997) is clearly present. We shall return to this point later.

As expected, the corrections are very similar to the curves shown in Figure 1. In addition to a general gray offset of $\sim 5\%$, there is also structure present at the $\sim 10\%$ level in all of the camera.

5.3. Pseudo-trail spectra

As mentioned in §3, the pseudo-trailed (p-trailed hereafter) spectra present a special problem since

there are not enough of them to perform a thorough analysis of their time and *THDA* systematics. Table 2 shows that there are only 18 LWP, 11 LWR and 35 SWP p-trail spectra for the standards. These include spectra with both 2 and 3 exposures in the large aperture. These subsets do not expose the same pixels in exactly the same way and there is no a priori reason to assume their corrections will be similar. However, we are forced to assume that they are, since we lack the data to determine otherwise. This situation is unfortunate, since in spite of the paucity of p-trail data for the standards, it was a popular observing mode, and there are many p-trail spectra in the archive.

Due to the lack of data, we had to adopted the following approach for calibration of the p-trail spectra. We assume that we know the intrinsic flux distributions for the p-trail spectra from either FOS spectra (if available), or mean values of fully corrected *IUE* large aperture data, transformed to the FOS system. Each p-trail spectrum was then divided by its corresponding FOS or mean *IUE* large aperture spectrum to produce a set of normalized spectra whose mean value should be unity. We then corrected the normalized p-trail spectra with both the large aperture and trailed temporal and *THDA* corrections and *IUE*–to–FOS calibration and compared the results.

We found that the large aperture corrections and calibration performed best in all cases; removing all obvious trends from the data, and reducing the overall scatter. They also produced a mean which was uniformly close to unity. This result was somewhat surprising, since the p-trails expose a wide swath of pixels, and one might expect their properties to be more similar to trailed spectra. However, it is possible that adjacency effects due to "beam pulling" dominate. If so, the multi-peaked cross-dispersion structure of the p-trail spectra may make their properties most similar to a single large aperture spectrum.

In any event, the RMS scatter of the normalized p-trail spectra (corrected by the large aperture relationships) from unity is $\sim 1\%$ over most of the usable range of the SWP and LWP, but there are regions where systematic deviations of $\sim 3\%$ may be present. For the LWR, the the scatter is uniformly $\sim 3\%$, but this is largely due to the overall poor photometric quality of the available LWR p-trails.

5.4. Special wavelength regions

There are wavelength regions for each camera where either the intrinsic data or our corrections algorithms are not well-defined. The wavelength extremes over which the corrections can be applied were determining by examining plots such as those shown in Figures 5a – 5c. These plots show that data for the longest wavelengths of the long wavelength cameras are poorly defined, and applying correction factors to these data has little meaning. Table 4 lists the wavelength range over which our correction factors are considered reliable for each camera. The factors are set to unity outside these regions.

There are also some specific wavelength regions which are problematic. However, most of these should not be a real concern, since they are flagged by the ν-Flags as being poor quality data. However, if the correction algorithm is blindly applied, it will produce a number for such data. Therefore, we caution users of our correction scheme to always use the ν-Flags to eliminate problematic data points.

One region which is *not* flagged by the ν-Flags, but is unreliable is the region near Ly α in the SWP data. The NEWSIPS spectral extraction uses a low order polynomial to represent the background on either side of the spectrum. This approach cannot handle Geocoronal Ly α emission which fills the aperture in long exposures. As a result, long exposures will be contaminated by Ly α emission over a spectral region equal to the projected size of the aperture used to obtain the data. These ranges are 1207 – 1222 Å for large aperture are trailed data and 1210 – 1221 Å for small aperture data. NEWSIPS low dispersion data cannot be trusted in these regions, and the corrections have been set to unity over them.

Finally, we note that Garhart et al. (1997) demonstrate that the NEWSIPS SWP spectra show an anomaly near 1515 Å. However, this problem appears to be significantly reduced in the corrected data, and we no longer consider it to be a major problem.

6. Verification

We now must verify the temporal and thermal corrections and the flux transformations derived in the previous section. In doing so, it is mandatory that we use only spectra that were not employed to derive the relationships. Since the best data sets were used to derive the relations, we cannot expect to test the full accuracy of the results.

We begin with verification of the temporal and *THDA* corrections. We use BD+33°2642 for verification since it and HD 93521 have the most data of the stars not used in deriving the temporal and *THDA* corrections. Figure 7 compares ratios of means of BD+33°2642 spectra obtained early in the mission to means of spectra taken late in the mission. Each set of ratios is labeled by the camera used to obtain the spectra. The dotted curves are ratios of uncorrected NEWSIPS data and the solid curves are ratios of NEWSIPS data corrected for temporal and *THDA* systematics. The SWP and LWP ratios are 50 spectra means and the LWR ratios are 20 spectra means. The mean time of each spectral mean is provided on the ordinate labels.

While (as expected from Figure 3 which uses far more data) the temporal corrections make little difference in the LWP data, they have 2 effects on the LWR and SWP spectra. In each case, the ratios of the corrected data are closer to unity (much more so for the LWR data) and much of the point-to-point variation is reduced in the corrected data, demonstrating that it was not true noise, but rather systematic effects.

We now turn to verification of the flux transformation. Figures 8a -8c compare the fully corrected and uncorrected NEWSIPS data for all of our program stars. We begin by examining specific improvements in the spectra of stars used to derive the transformations and then turn to those stars used to verify the results.

The improvements for the stars used to derive the transformation (BD+75°375, BD+28°4211, BD+33° 2642, and G191B2B) are truly spectacular. In particular,

1. Reduction of point-to-point "noise" is most noticeable in the long wavelength cameras. In particular, the He I lines in BD+28°4211 and BD+75°375 are much more distinct. In fact, these lines are barely visible in the uncorrected NEWSIPS LWR spectra of BD+75°375, but are obvious in the corrected spectra.

2. The 1515 Å artifact (Garhart et al. 1997) is clearly present in the NEWSIPS spectra of BD+28°4211, BD+33°2642 and G191B2B, but it is reduced or completely removed in the corrected spectra.

3. Structure in the region $2200 < \lambda < 2500$ Å in the LWP spectra of G191B2B is removed.

We must seek verification of these results in the stars which did not enter into the derivation of the relationships. We are at a bit of a disadvantage here, since the white dwarfs not included in the derivations are not well observed and the OB stars have rather "busy" spectra. Nevertheless, the following are clearly seen:

1. The point-to-point "noise" is clearly reduced in the corrected SWP spectra of HD 60753 and dramatically reduced in the LWP and LWR spectra of HD 93521 and HD 60753.

2. The 1515 Å feature clearly reduced in the SWP spectra of GD 153, GD 71 and HD 60753. It is also reduced in HD 93521, but it is difficult to see since it lies in a strongly blanketed region of its spectrum. Given the vastly different flux levels and temporal distributions of these observations, the possibility that this artifact is completely removed by the corrections is quite good.

3. The structure between 2200 and 2500 Å in the LWP spectra of GD 153 and GD 71 is reduced in the corrected data. Its removal is not so apparent in LWP spectra of HZ 43 and HZ 44 because of their higher noise level (see their FOS spectra).

Finally, Figures 9a-9c compare the fully corrected NEWSIPS data with the FOS data. The FOS data have been degraded to match the *IUE* spectral resolution. For the 3 calibration stars with the most data, it is almost impossible to distinguish between the FOS and *IUE* spectra. It is also clear that the corrected *IUE* spectra the 4 stars not used in the calibrations agree their FOS counterparts quite well. The only exceptions are near Ly α in GD 153 and GD 71. That disagreement arises because these were relatively long exposures, so the region of Ly α is partly filled in by geo-coronal emission (see §5.4).

We see, therefore, that the improvements provided by the new calibrations are also present in spectra which were not used to derive the relationships. This independent verification of our results provides confidence in their veracity.

7. Error analysis

To quantify the significance of an observed feature or the accuracy of a flux level, two types of error must be evaluated: random and systematic errors. Broadly speaking, the random errors are due to uncontrollable effects which change in an unpredictable manner from one exposure to the next. They can be either point-to-point errors (e.g., photometric errors) or broad band errors (e.g., the scaling errors discussed in §3). An important aspect of random errors is that they can be "averaged down", i.e., the average of N observations repeated under similar conditions is $1/\sqrt{N}$ times more accurate than any one of the observation. On the other hand, systematic errors depend upon some specific factor (e.g., exposure level), are typically broad band, and cannot be averaged down, since the entire data set is subject to their influence. This does not mean, however, that they cannot be over come. The corrections we have derived for the temporal *THDA* systematics are examples of correctable systematic errors.

7.1. random errors

We begin by characterizing the random errors. This will first be done in a qualitative manner, using the same approach adopted by NL. However, we use HD 93521 as our test object because it was not used in the derivation of either the temporal or flux corrections, making it an unbiased data set. Further, there are enough observations of the star to determine whether the random S/N truly asymptotes. On the negative side, HD 93521 is known to have variable wind lines (e.g., Howarth and Reid 1993, Massa 1995), and its spectrum is rather "busy", containing considerable structure.

The S/N was calculated exactly as outlined by NL. First we summed n spectra (where n varies from 1 to the the total number in the sample) drawn at random from the sample. Next, we calculated means and standard deviations over 4 point bins (roughly a resolution element). These were then converted into S/N ratios and summed over specified wavelength regions to obtain the final results. The wavelength regions selected were $1400 < \lambda < 1500$ Å and $1650 < \lambda < 1900$ Å for the SWP and $2200 < \lambda < 2900$ Å for the long wavelength cameras. These regions are comprised of the most responsive portions of the cameras and the SWP region avoids variable wind lines.

Figure 10 shows the results of the analysis for both the uncorrected and corrected NEWSIPS data. While there is only a modest improvement for the SWP data, the improvement for the long wavelength camera data is quit dramatic. The figure also shows that the LWR camera is the most "intrinsically" noisy of the 3, with a maximum attainable $S/N \sim 40:1$, followed by the SWP with a maximum $S/N \sim 60:1$ and the LWP being the best with a maximum $S/N \sim 80:1$. The figure also demonstrates that there is little to gain in summing more than ~ 10 *IUE* spectra, but up to that point, the gain is considerable.

We next consider a more quantitative description of the errors. This is done by comparing the observed errors (the standard deviations derived from the repeated observations of the standard stars) to the NEWSIPS error model, whose results are given in the error vector in the NEWSIPS data files. Both of these are calculated as unweighted statistics, since the overall quality of the individual spectra are relatively uniform. Only data points without a known problem (ν-Flag = 0) or on the extrapolated ITF (ν-Flag = -128 and -256) were included in each calculation.

Figure 11 shows ratios of the observed standard deviations, $\sigma(Obs)$, to errors derived from the NEWSIPS error models, $\sigma(NEWSIPS)$, for the 3 standard stars; HD 60753, BD +28°4211 and BD+75°375. The $\sigma(NEWSIPS)$ are simply the square root of the quadratic mean of the NEWSIPS error arrays for all the good data points at each wavelength, while the $\sigma(Obs)$ are the standard deviations of all the good points at each wavelength. Each panel shows a different camera–observing mode combination. There are 2 curves in each panel. One is the mean $\sigma(Obs)$ for the 3 standards using unscaled observations and the other is the mean $\sigma(Obs)$ derived from spectra which were rescaled to agree over the fixed wavelength bands described in §5. For the large aperture data, these 2 curves are nearly indistinguishable, since the scaling errors discussed in §3 are nearly negligible. On the other hand, the two curves are well separated for the trailed data and very distinct for the small aperture data, with the unscaled observations always producing larger errors.

In every case, the NEWSIPS error model underestimates the actual errors. The amount is typically of order unity for the large aperture and trailed data, but more than a factor of 2 for the small aperture scaled data.

Table 5 lists the RMS scatter in the scaling factor as a fraction of the flux across the bands given

in §5 for each camera – observing mode combination. It also gives the mean $\sigma(Obs)/\sigma(NEWSIPS)$ ratio for each camera – observing mode combination (with and without normalization). These numbers will be useful guides when carrying out quantitative error analyses with NEWSIPS spectra, although it must be remembered that the ratios sometimes contain considerable shape, so their characterization as a single number can be an over simplification.

7.2. systematic errors

There are two additional parameters provided in with the NEWSIPS data files that can be used to search for systematic effects. These are exposure times and exposure levels.

Since longer exposures typically have higher background counts, it is possible that there could be systematics in the data which are related to the exposure time used to obtain the spectrum. However, the results of Figures 9a-9c argue against such a systematic. The quality of the agreement between *IUE* and FOS data for the stars shown in the figure is excellent for stars with exposure times as short as 4 sec (for the SWP) and 6 sec (for the LWR and LWP) to as long as 21 minutes for the LWR and 30 minutes for the LWP and SWP. So we can be confident that the data are free of exposure time dependent systematics over this range of exposure times.

Finally, we examined the data for systematic differences between spectra of the same star exposure to levels. For this purpose, we used the net spectra in the NEWSIPS data files, which are expressed in linearized flux units, *FN*s (see Garhart et al. 1997). Systematic differences between spectra exposed to different mean *FN*s would indicate a problem with the Intensity Transfer Function (ITF) which transforms the observed counts (in data units, *DN*s), into the linearized *FN*s.

To search for an ITF problem, we examined spectra of the same star obtained with different exposure times, making sure that saturated pixels were eliminated from the comparison. Although no major ($\geq 3\%$) systematics were uncovered in the SWP and LWR data, the LWP spectra do contain sizable ITF systematics. Figure 12 shows exposure level systematics for LWP spectra of BD+28°4211, HD 60753, and BD+75°375. The plot shows mean NEWSIPS fluxes over the wavelength band $2350 < \lambda < 2400$Å (the peak of the LWP camera response) for each star. These have been normalized by the mean of all exposures with $200 < FN < 400$ (saturated pixels *and* pixels using an extrapolated ITF were eliminated). Observations of the same star with very different mean *FN*s result from different exposure times. The fact that fluxes derived from long exposure times (large *FN* values) are systematically larger (by about 5%) than fluxes derived from low *FN*s indicates a problem with the LWP ITF (since we have already ruled out systematics which depend solely on exposure time). This means that a comparison of an optimal exposure and a half optimal exposure of stars with similar energy distributions will contain systematic errors up $\sim 5\%$.

Figure 13 shows how the ITF problem can also affect the shape of an energy distribution. It displays ratios of long and short exposures of BD+28°4211 (full curve), HD 60753 (dotted curve), and BD+75°375 (dashed curve). The ratios consist of mean spectra derived from spectra whose mean *FN* over the band $2650 < \lambda < 2700$ Å lie in the range $200 << FN >< 400$, divided by means of spectra with $600 << FN >< 800$ over the same band. Data from saturated pixels and pixels using an extrapolated ITF were excluded from the means. It is clear from the figure how data near the peak of the camera response (between 2500 and 2850 Å) are systematically different by up to 5%.

The LWP ITF problem is not as severe as it first appears. It means that comparisons of well exposed and under exposed data may have systematics on the order of 5%. However, 5% is roughly the size of random errors for half optimal exposures (the reason the systematic effect shows up so well in Figure 13 is that hundreds of spectra went into the ratios), so the effect does not dominate the errors when comparing a single half optimal exposure to an optimal one (although it is comparable to the random errors). Another property that tends to suppress the effect is that the shape of the response curve dominates the shape of the net spectrum. Thus, as long as the intrinsic shapes of the objects being compared are not too different and as long as the spectra have similar exposure levels, the impact of the LWP ITF problem should not be too bad. However, it underscores our assertion that the results of the present paper strictly apply to early type stars only.

8. Summary and Conclusion

1. We have analyzed more than 4600 spectra to demonstrate that low dispersion NEWSIPS data contain systematic effects on the order of $10-15\%$ and to obtain corrections for these effects.

2. Systematics were reduced to $< 3\%$ in most instances, but can be as large as 5% in a few specific cases involving LWP data. Overall, we can hope for a $S/N \sim 30:1$ ($\sim 20:1$ for some LWP applications) but not more. To exceed this value one would have to consider recalibrating the ITFs, and even rederiving them from first principles.

3. Nevertheless, it may be possible to surpass the 3% level when dealing with relative measurements of a very homogeneous data set obtained over a relatively short period of time and under similar conditions.

4. We have derived a transformation between the corrected *IUE* data and the *HST* FOS absolute flux scale. The magnitude of the transformations can be larger than 10% at certain wavelengths.

5. We note that much of what appears to be noise in NEWSIPS spectra is actually the result of high frequency systematics and flux calibrations.

6. The random errors in the corrected NEWSIPS data are characterized in Table 5.

7. The pseudo trailed spectra are poorly characterized by the available data. However, application of the large aperture corrections and flux transformation appear to reduce their systematics to about the 3% level.

8. We emphasize that our results apply to NEWSIPS data for *blue objects*, and we cannot guarantee any broader application.

9. Finally, a set of IDL procedures which apply the results of this paper to NEWSIPS low dispersion spectra will be made available to the *IUE* RDAF project at the Space Telescope Science Institute and will be available from the authors on request.

We would like to thank Michael Van Steenberg and Nancy Oliversen for sharing their detailed knowledge of *IUE* data and how it is processed. We are also thankful to Patricia Lawton and Karen Levay for facilitating access to the data and to Joy Nichols for providing us with the model of G191B2B used by the *IUE* project to calibrate the data. We also acknowledge support through NASA contract NAG5-7372 to Raytheon STX and Grant NAG5-7113 to Villanova University.

REFERENCES

Ayers, T.R. 1993, PASP, 105, 538

Bless, R.C. & Percival, J.W. 1998, in Proc. of IAU Symp. 189 "Fundamental Stellar Properties: The Interaction between Observation and Theory", eds. T.R. Bedding, A.J. Booth & J. Davis, (Kluwer, Dordrecht), p73

Boggess, A. et al. 1978, Nature, 275, 372

Bohlin, R.C. 1996, AJ, 111, 1743 (B96)

Fitzpatrick, E.L. & Massa, D. 1999, in preparation

Garhart, M.P, Smith, M.A., Levey, K.L. & Thompson, R.W. 1997, "*International Ultraviolet Explorer* New Spectral Image Processing System Information Manual Version 2.0", NASA *IUE* Newsletter No. 57

Howarth, I.D. & Reid, A.H.N. 1993, A&A, 279, 148

Kurucz, R.L. 1991, in "Stellar Atmospheres – Beyond Classical Models", eds. L. Crivellari, I. Hubeny & D.G. Hummer, (Kluwer, Dordrecht), p.441

Massa, D. 1995, ApJ, 438, 376

Massa, D., Van Steenberg, M.E., Oliversen, N. & Lawton, P. 1998, in "Ultraviolet Astrophysics Beyond the *IUE* Final Archive", eds. Wamsteker and Riestra, (ESA SP-413, ESA Pubs. Div., Noordwijk, The Netherlands), p723

Newmark, J.S., Holm, A.V., Imhoff, C.L., Oliverson, N.A., Pitts, R.E. & Sonneborn, G. 1992, "*IUE* Observing Guide", NASA *IUE* Newsletter No. 47

Nichols, J.S. & Linsky, J.L. 1996, AJ, 111, 517 (NL)

Pérez, M.R., Oliversen, N., Garhart, M. & Teays, T. 1990, in "Evolution in Astrophysics", ed. E.J. Rolfe, (ESA SP-310, ESA Pubs. Div., Noordwijk, The Netherlands), p349

This 2-column preprint was prepared with the AAS LaTeX macros v4.0.

TABLE 1
PROGRAM STARS

Star	Spectral Type	V	$B-V$	Temporal/ Thermal Standard	Temporal/ Thermal Control	Flux Standard	Flux Control
HD 60753	B3 IV	6.69	-0.09	×	–	–	×
HD 93521	O9.5Vn	7.04	-0.28	–	×	–	×
BD+28°4211	sdO	10.52	-0.33	×	–	×	–
BD+75°325	sdO	9.54	-0.37	×	–	×	–
BD+33°2642	B2 IVp	10.84	-0.17	–	×	×	–
G191B2B	DA	11.78	-0.34	–	×	×	–
GD 71	DA	13.04	-0.24	–	–	–	×
GD 153	DA	13.42	-0.25	–	–	–	×
HZ 43	DA	12.86	-0.10	–	–	–	×
HZ 44	DA	11.71	-0.27	–	–	–	×

TABLE 2
SPECTRA

Star	Camera	Observation Mode	t_{min} (sec)	t_{max} (sec)	Number of Spectra Used in Analysis
HD 60753	LWP	lg apt	4	8	258
	–	trail	10	50	212
	–	sm apt	8	20	98
		p-trail	–	–	7
HD 60753	LWR	lg apt	4	20	79
	–	trail	8	45	77
	–	sm apt	5	22	52
		p-trail	–	–	2
HD 60753	SWP	lg apt	6	12	321
	–	trail	10	75	270
	–	sm apt	10	30	145
		p-trail	–	–	11
HD 93521	LWP	lg apt	2	4	114
	–	trail	7	16	23
	–	sm apt	5	10	16
		p-trail	–	–	2
HD 93521	LWR	lg apt	2	4	68
	–	trail	12	20	11
	–	sm apt	4	10	48
		p-trail	–	–	1
HD 93521	SWP	lg apt	2	4.5	171
	–	trail	10	20	34
	–	sm apt	4	9	61
		p-trail	–	–	2
BD+28°4211	LWP	lg apt	25	55	244
	–	trail	90	500	36
	–	sm apt	75	160	51
		p-trail	–	–	4
BD+28°4211	LWR	lg apt	30	80	81
	–	trail	100	450	16
	–	sm apt	40	190	46
	–	p-trail	–	–	4
BD+28°4211	SWP	lg apt	20	60	350
	–	trail	40	160	55
	–	sm apt	20	90	100
	–	p-trail	–	–	7
BD+33°2624	LWP	lg apt	120	220	120
	–	trail	–	–	1
	–	sm apt	300	600	4
	–	p-trail	–	–	3
BD+33°2624	LWR	lg apt	80	200	54
	–	trail	–	–	1
	–	sm apt	200	500	13
	–	p-trail	–	–	3

TABLE 2—*Continued*

Star	Camera	Observation Mode	t_{min} (sec)	t_{max} (sec)	Number of Spectra Used in Analysis
BD+33°2624	SWP	lg apt	150	350	179
	–	trail	–	–	3
	–	sm apt	250	500	14
	–	p-trail	–	–	9
BD+75°375	LWP	lg apt	10	30	248
	–	trail	40	180	50
	–	sm apt	30	70	72
	–	p-trail	–	–	2
BD+75°375	LWR	lg apt	10	35	77
	–	trail	20	100	20
	–	sm apt	25	75	50
	–	p-trail	–	–	1
BD+75°375	SWP	lg apt	12	36	321
	–	trail	15	110	77
	–	sm apt	15	45	116
	–	p-trail	–	–	3
G191B2B	LWP	lg apt	–	–	36
	–	sm apt	–	–	2
G191B2B	LWR	lg apt	–	–	1
	–	trail	–	–	1
G191B2B	SWP	lg apt	–	–	34
	–	trail	–	–	14
	–	sm apt	–	–	5
	–	p-trail	–	–	4
GD 71	LWP	lg apt	–	–	8
GD 71	LWR	lg apt	–	–	1
GD 71	SWP	lg apt	–	–	7
	–	sm apt	–	–	2
	–	p-trail	–	–	4
GD 153	LWP	lg apt	–	–	8
GD 153	LWR	lg apt	–	–	2
GD 153	SWP	lg apt	–	–	10
	–	sm apt	–	–	2
HZ 43	LWP	lg apt	–	–	1
HZ 43	LWR	lg apt	–	–	5
	–	sm apt	–	–	2
HZ 43	SWP	lg apt	–	–	9
	–	sm apt	–	–	4
	–	p-trail	–	–	4
HZ 44	LWP	lg apt	–	–	3
HZ 44	LWR	lg apt	–	–	1
HZ 44	SWP	lg apt	–	–	7

Table 3
LWP/LWR Wavelength Corrections

λ (Å)	$\Delta\lambda$ (Å)
1800	-2.50
1950	-2.50
2200	-2.00
2250	-1.75
2300	-1.50
2385	-1.00
2510	-0.40
2730	0.00
3500	0.00

Table 4
Wavelength Ranges

Camera	Range
LWP	1950 – 3150 Å
LWR	1850 – 3150 Å
SWP	1150 – 1978 Å

Table 5
RMS errors and scale factors

Camera	Observing mode	Scaling error	$\sigma(Obs)/\sigma(NEWSIPS)$ un-normalized	$\sigma(Obs)/\sigma(NEWSIPS)$ normalized
LWP	Large Apt	0.020	1.15	1.12
	Trailed	0.025	1.44	1.24
	Small Apt	0.304	7.93	2.69
LWR	Large Apt	0.038	1.11	1.09
	Trailed	0.036	1.18	1.03
	Small Apt	0.180	3.91	2.01
SWP	Large Apt	0.018	1.28	1.23
	Trailed	0.021	1.49	1.30
	Small Apt	0.264	10.3	2.68

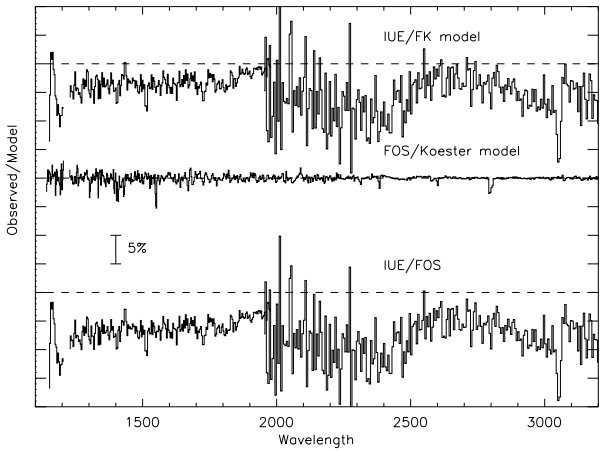

Fig. 1.— Ratios of white dwarf models and observations. The top panel shows the ratio of the mean *IUE* NEWSIPS data for G191B2B divided by the Finley & Koester model used to define the NEWSIPS calibration. The middle panel if the ratio of the *HST* FOS observations of G191B2B and the Koester model used in the calibration of the FOS. The bottom panel is the ratio of the NEWSIPS data divided by the FOS data.

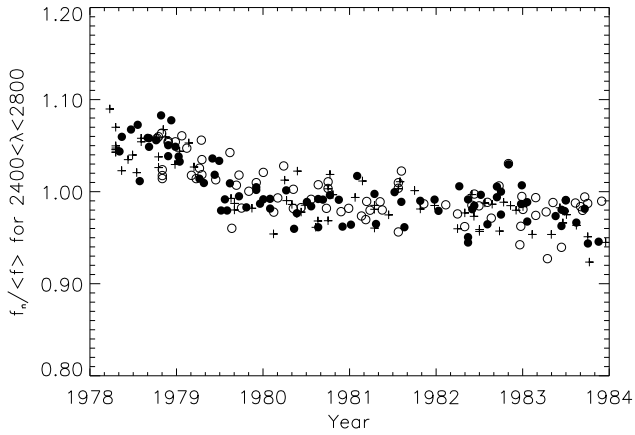

Fig. 2.— Time dependence of standard star fluxes in the LWR camera. This figure shows the mean flux over the wavelength band $2400 < \lambda < 2800$ Å from normalized by its mean value for 3 *IUE* standard stars; HD 60753, BD+28°4211 and BD+75°375. The mean flux was determined for each standard star observation then divided by the sample mean for that star. The 3 sets of relative fluxes were then overploted, with crosses for HD 60753, filled circles for BD+28°4211, and open circles for BD+75°375.

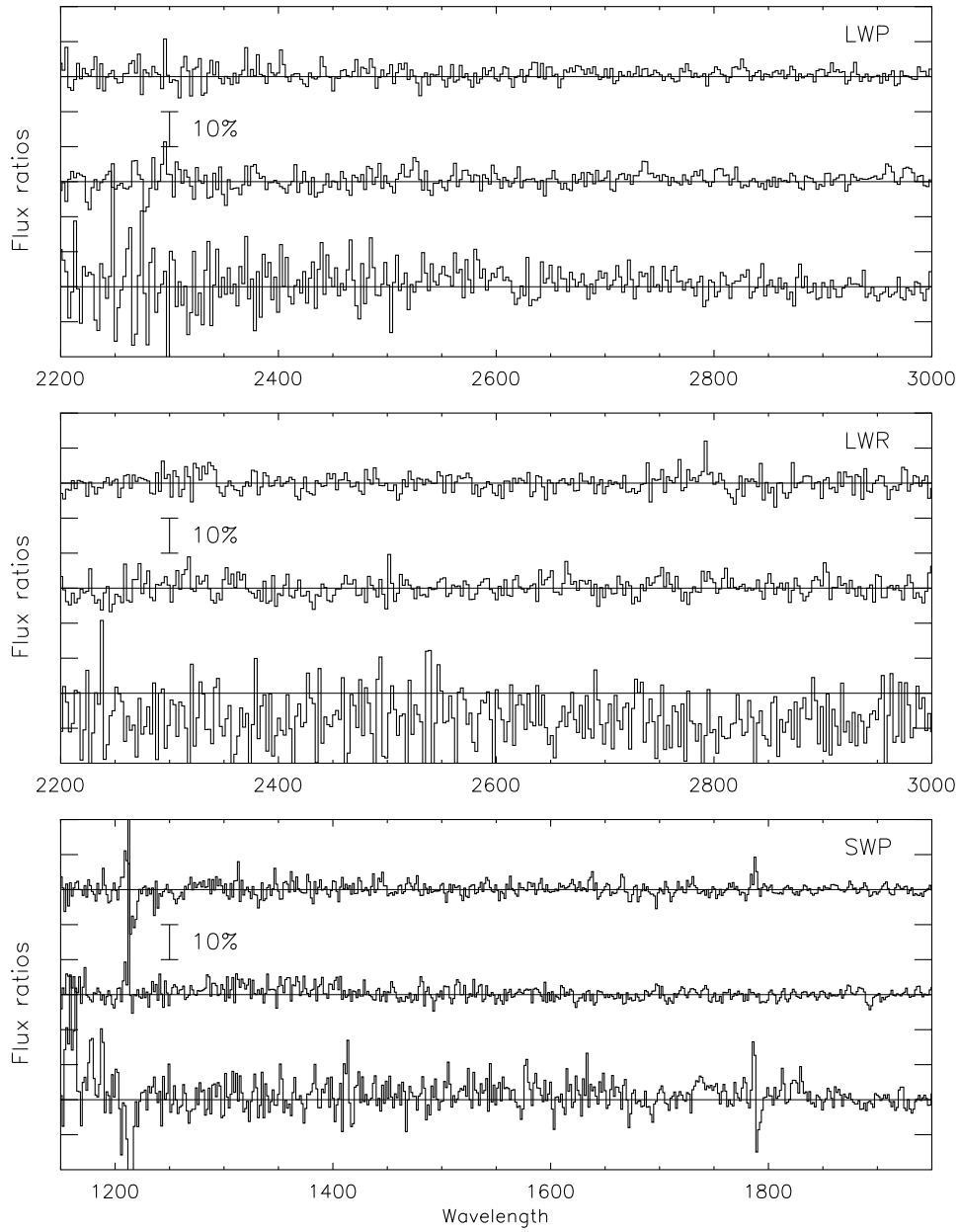

Fig. 3.— This figure demonstrates the presence of high frequency (in wavelength) time dependent systematics in the *IUE* NEWSIPS data (see §1).

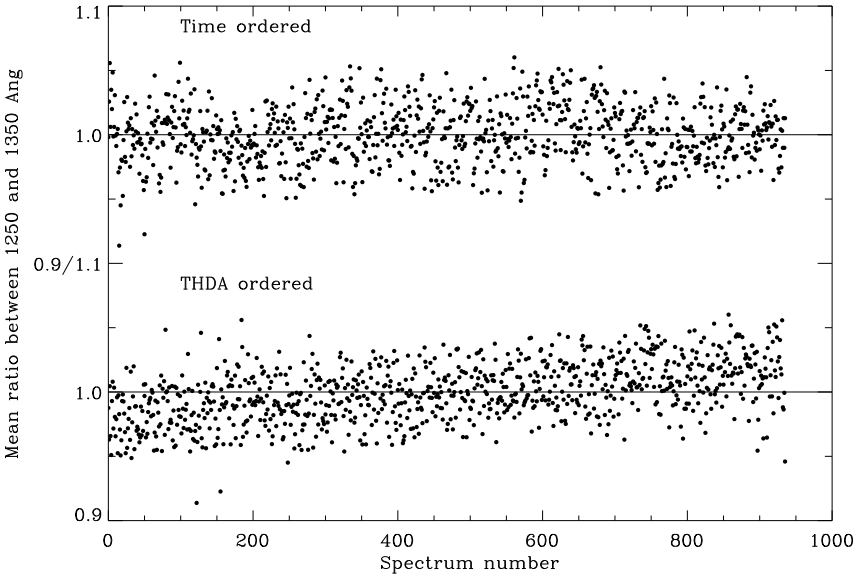

Fig. 4a.— Normalized SWP fluxes of *IUE* standard stars binned over the wavelength band $1250 \leq \lambda \leq 1350$. The upper plot shows the data arranged chronologically, and the lower plot shows them arranged in order of ascending *THDA* value.

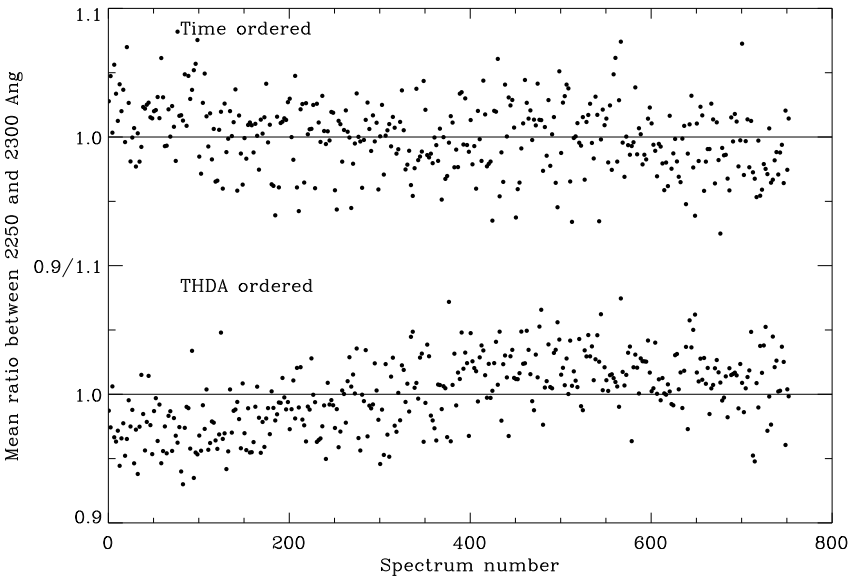

Fig. 4b.— Same as 4a, for LWP data binned over the wavelength range $2250 \leq \lambda \leq 2300$. In this case, adjoining points were averaged to reduce the larger noise level due to the smaller wavelength band used to demonstrate the effect.

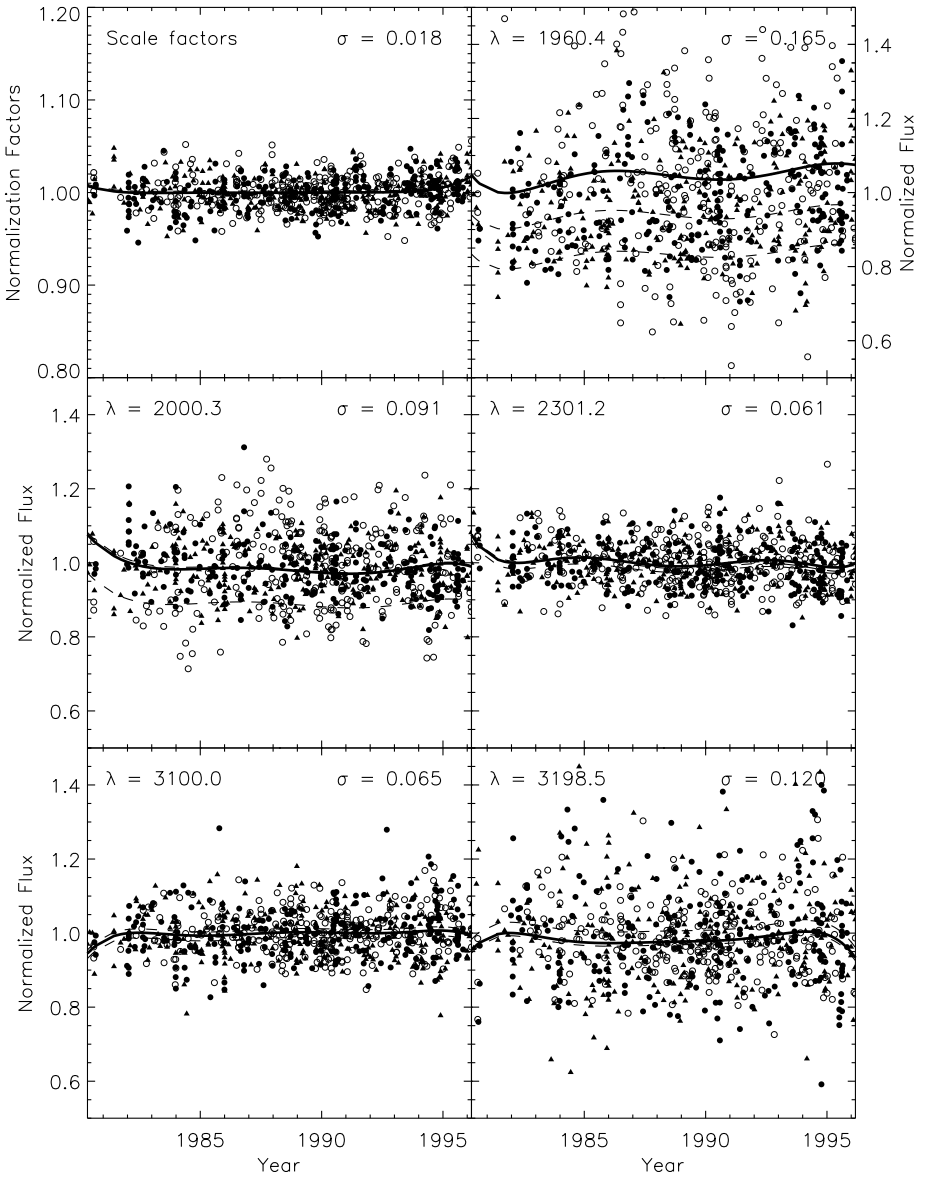

Fig. 5a.— Examples of fits of the model to the time dependent systematics of the LWP data. The fits shown are for $THDA = THDA_0$, with dashed curves indicating ± 0.75 of the full range in *THDA*. The upper left panel shows the fit to the relative scale factors, and the next 5 panels show fits to the data at selected wavelengths (listed on the figure). The wavelengths are the means of 3 *IUE* adjoining wavelength points to reduce the overall scatter. Each panel also lists the standard deviation of the 3 channel mean fit or the scale factors, σ. Data from the different stars are keyed as follows: HD 60753 – open circles, BD+28°4211 – filled circles, BD+75°375 – filled triangles.

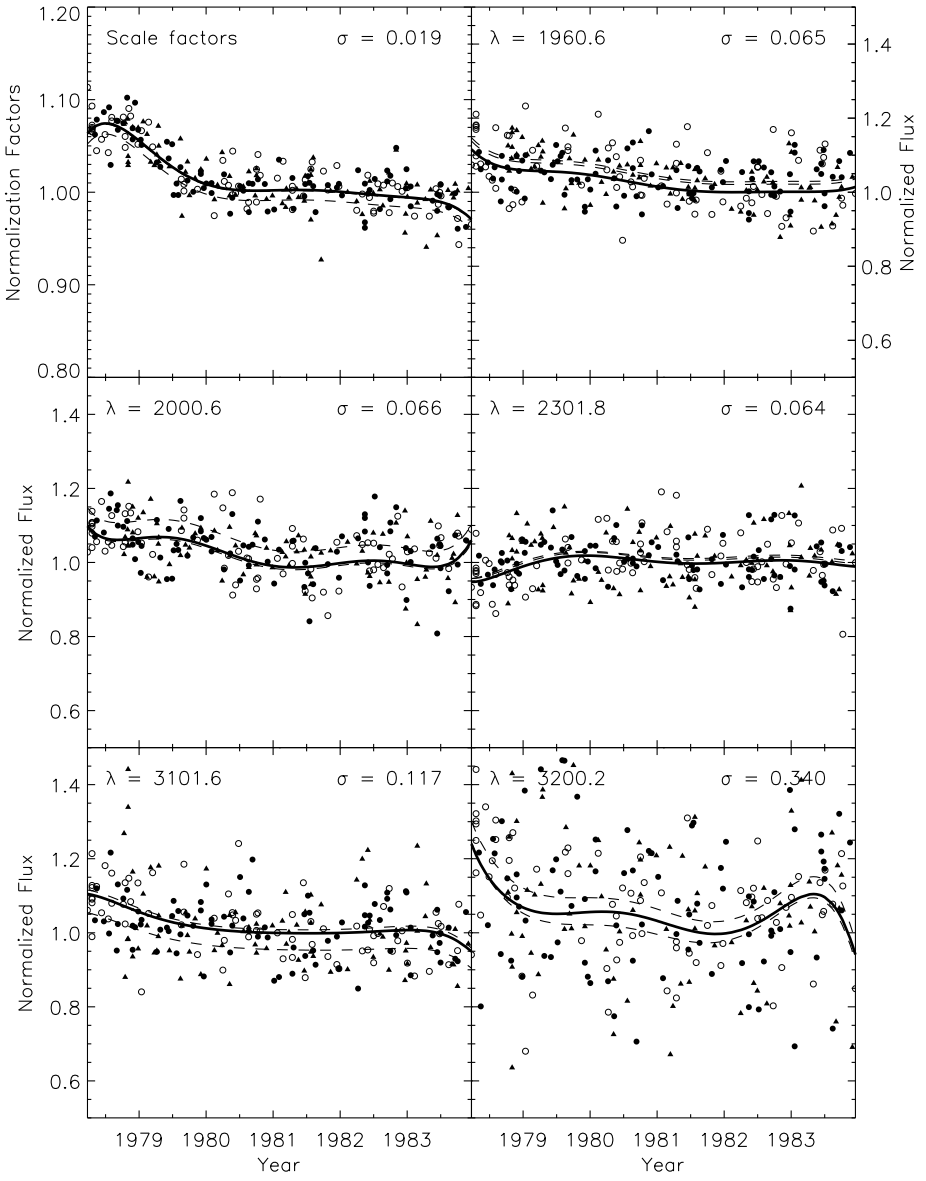

Fig. 5b.— Same as Figure 5a, for LWR data.

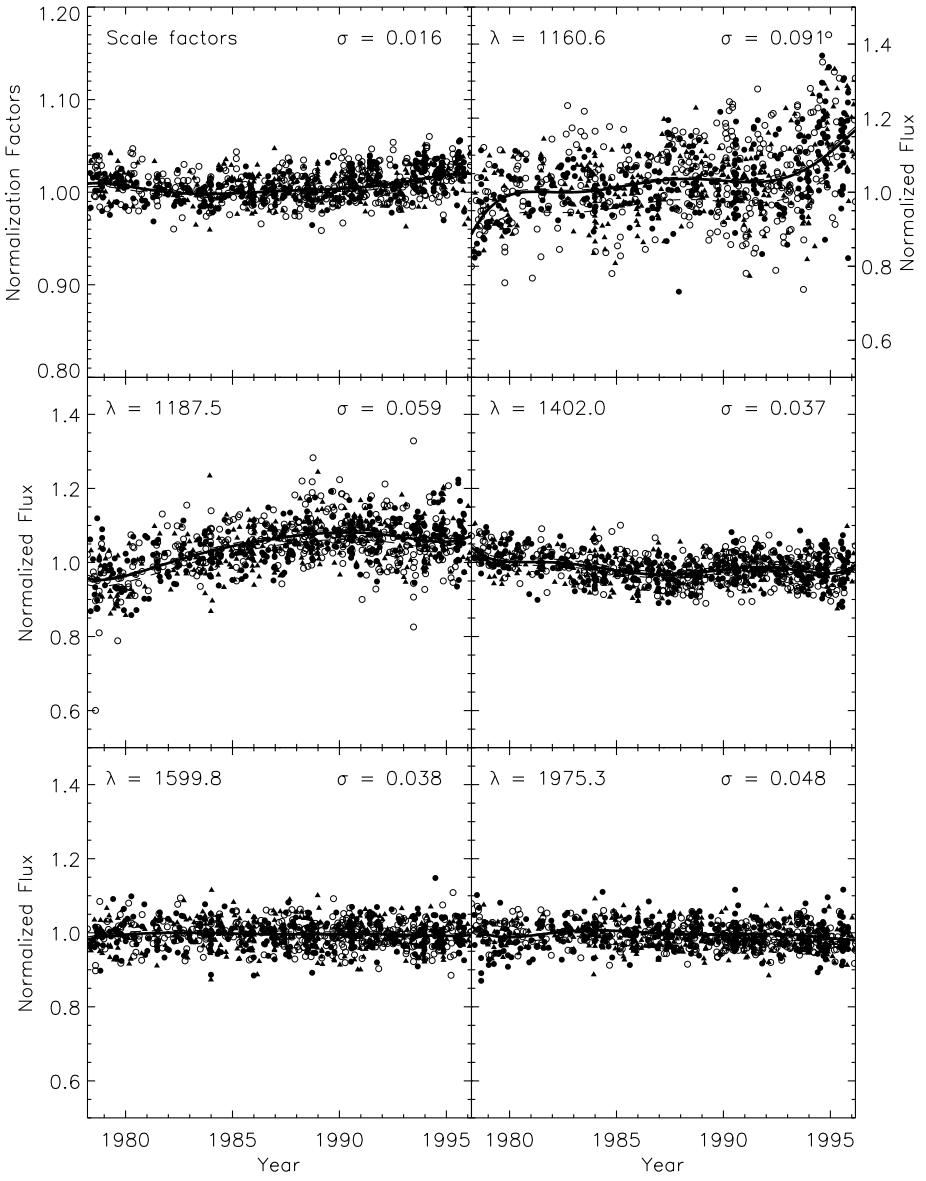

Fig. 5c.— Same as Figure 5a, for SWP data.

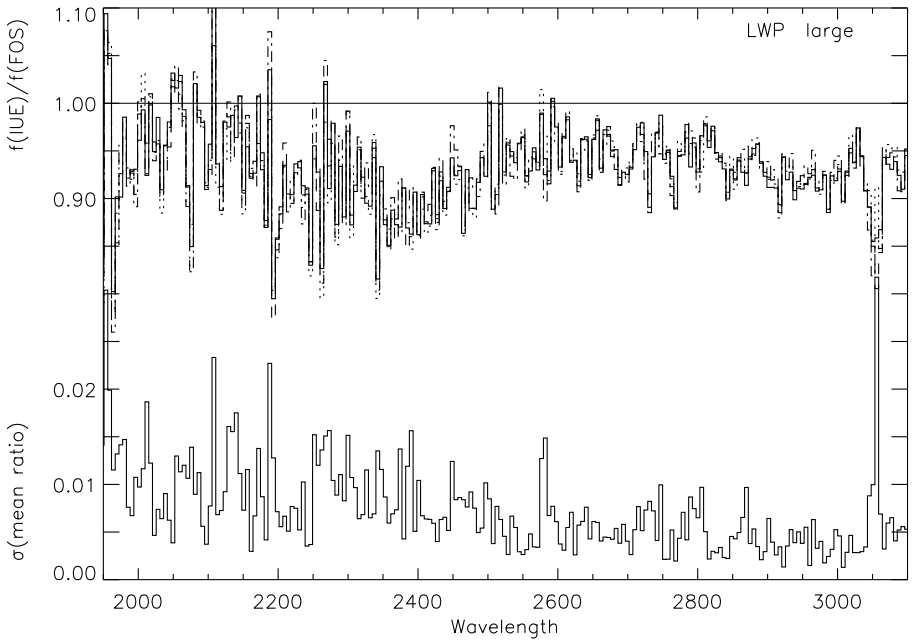

Fig. 6a.— Ratios of fully corrected mean LWP large aperture spectra divided by FOS spectra for the 4 standard stars used to derive the absolute flux transformation (see Table 1). The *IUE* wavelength scale was adjusted to agree with the FOS scale prior to the division. Two point binning was applied to the data for display. The individual ratios are depicted by different curves: solid for BD+28°4211, dotted for BD+75°375, dashed for BD+33°2642, and dot-dashed for G191B2B. The standard deviation of the weighted mean of the 4 curves is shown at the bottom.

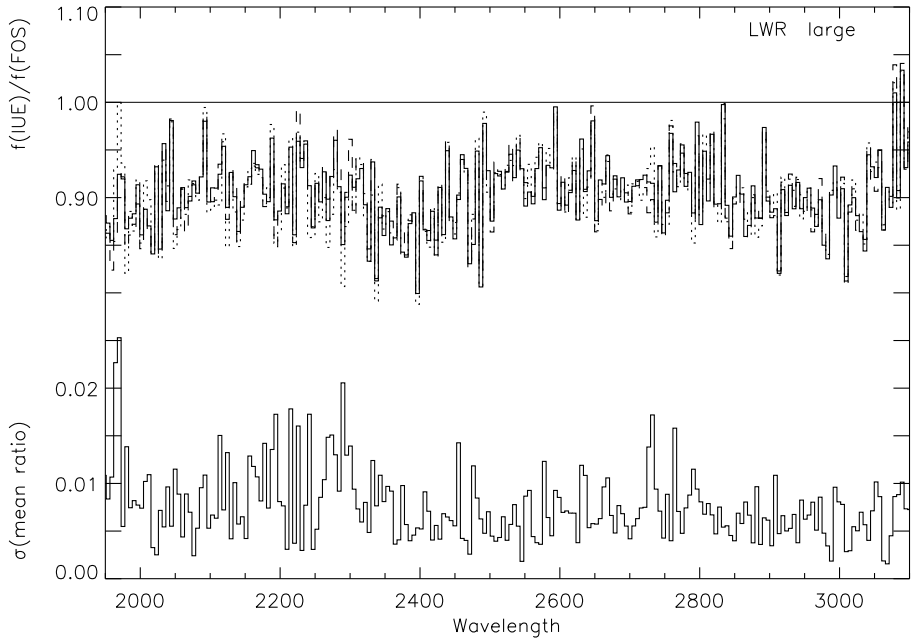

Fig. 6b.— Same as Figure 6a for LWR data. G191B2B is excluded due to a paucity of data.

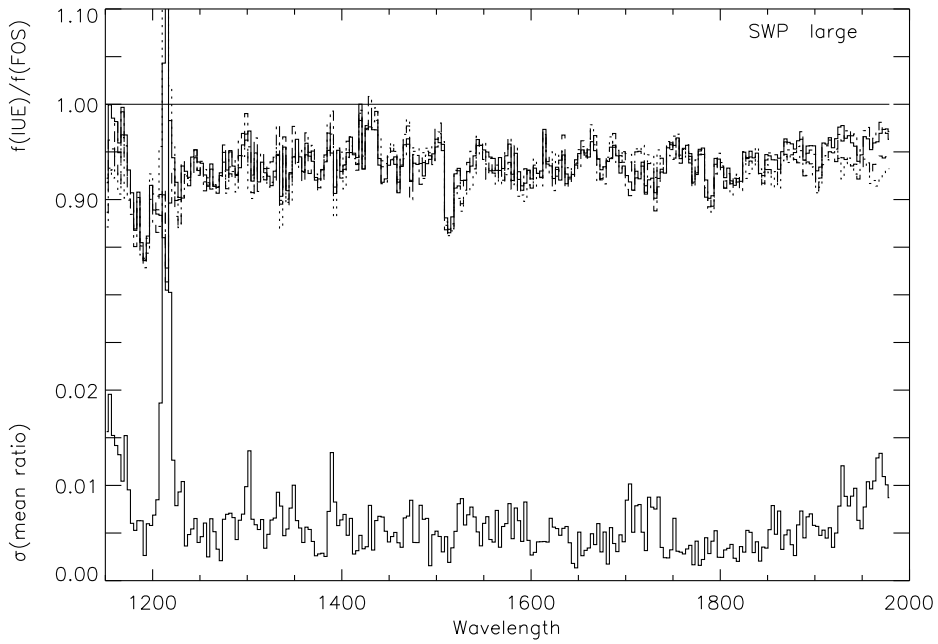

Fig. 6c.— Same as Figure 6a for the SWP data.

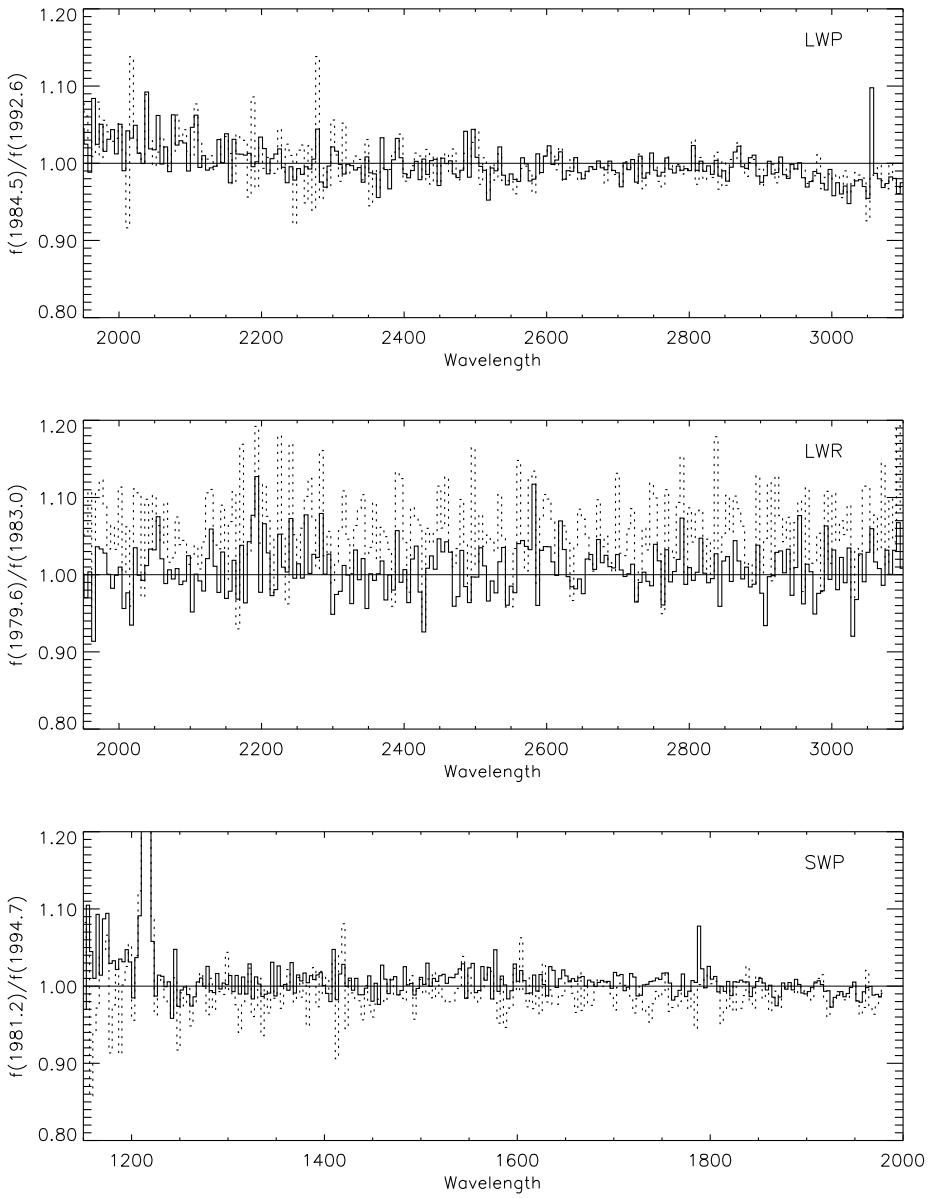

Fig. 7.— Ratios of means of spectra obtained early in the mission to means of spectra taken late in the mission for BD+33°2642. Each set of ratios is labeled by the camera used to derive them. The dotted curves are ratios of uncorrected NEWSIPS data and the solid curves are ratios of NEWSIPS data corrected for systematics. The SWP and LWP ratios are 50 spectra means and the LWR ratios are 20 spectra means. The mean time of the spectra are given on the ordinate labels.

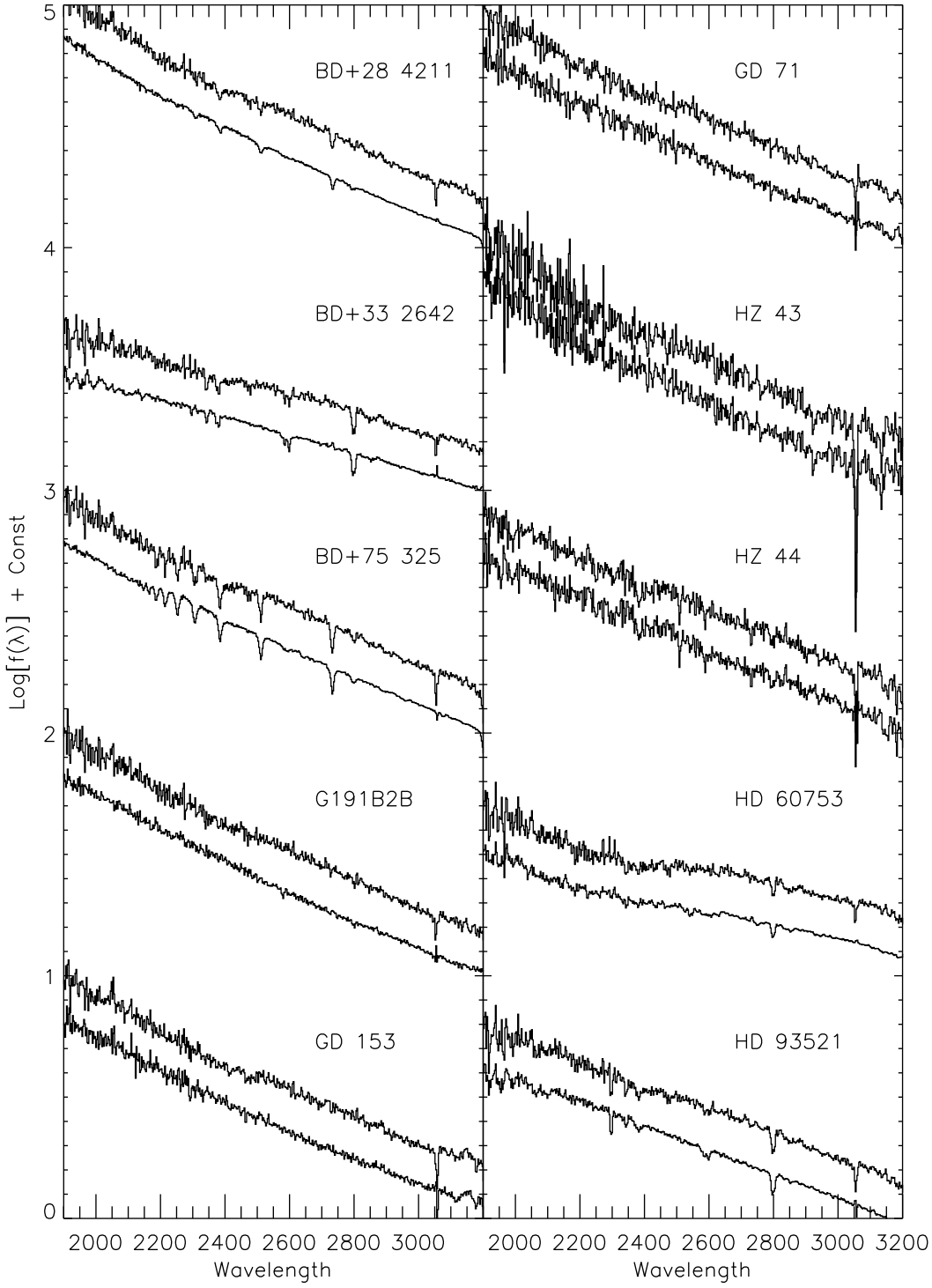

Fig. 8a.— Comparison of NEWSIPS and fully corrected NEWSIPS LWP data. Each pair of plots has the original, uncorrected NEWSIPS fluxes above the fully corrected data transformed to the FOS flux scale.

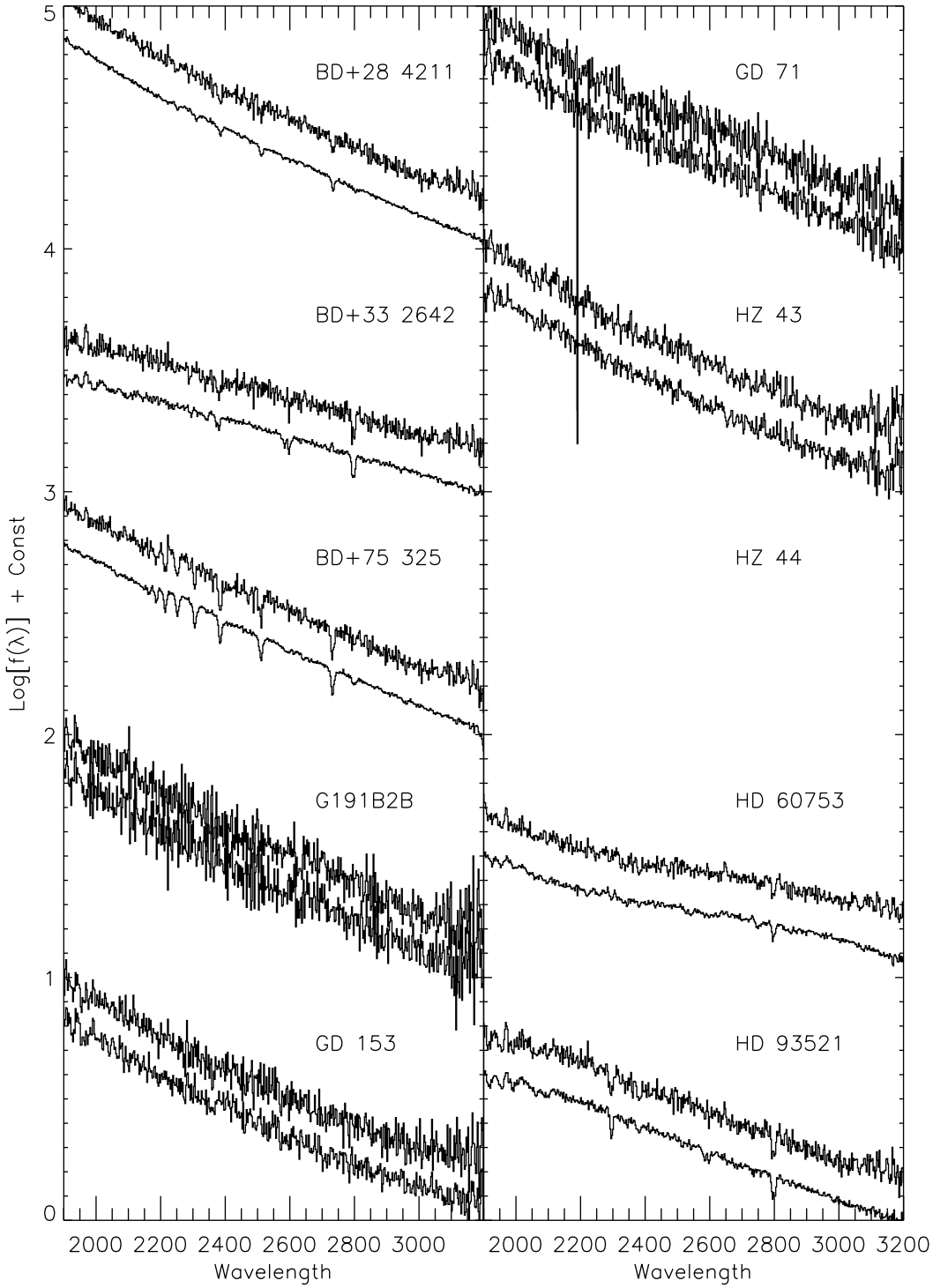

Fig. 8b.— Same as Figure 8a for the LWR data. There are no LWR large aperture data for HZ 44.

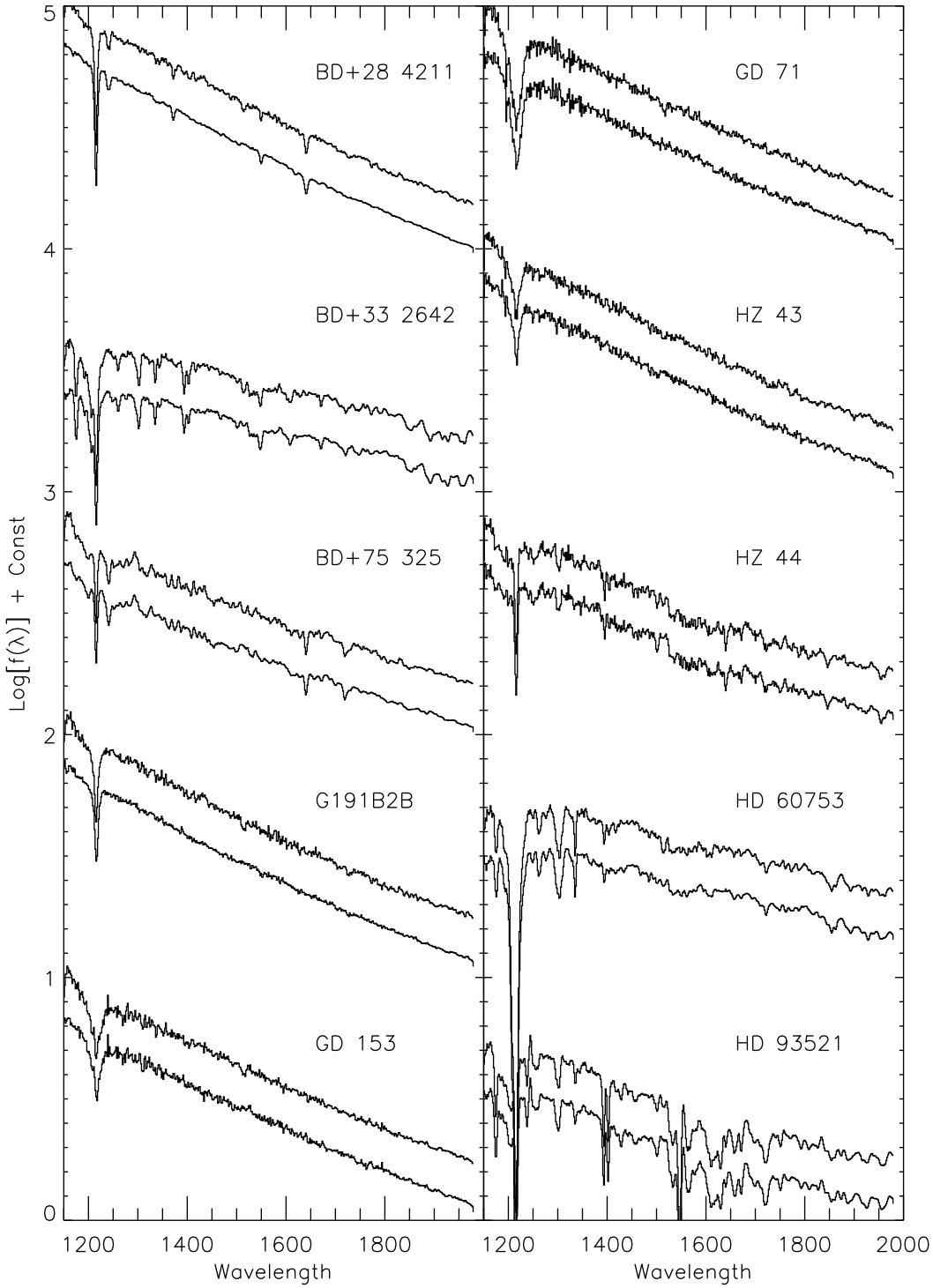

Fig. 8c.— Same as Figure 8a for the SWP data.

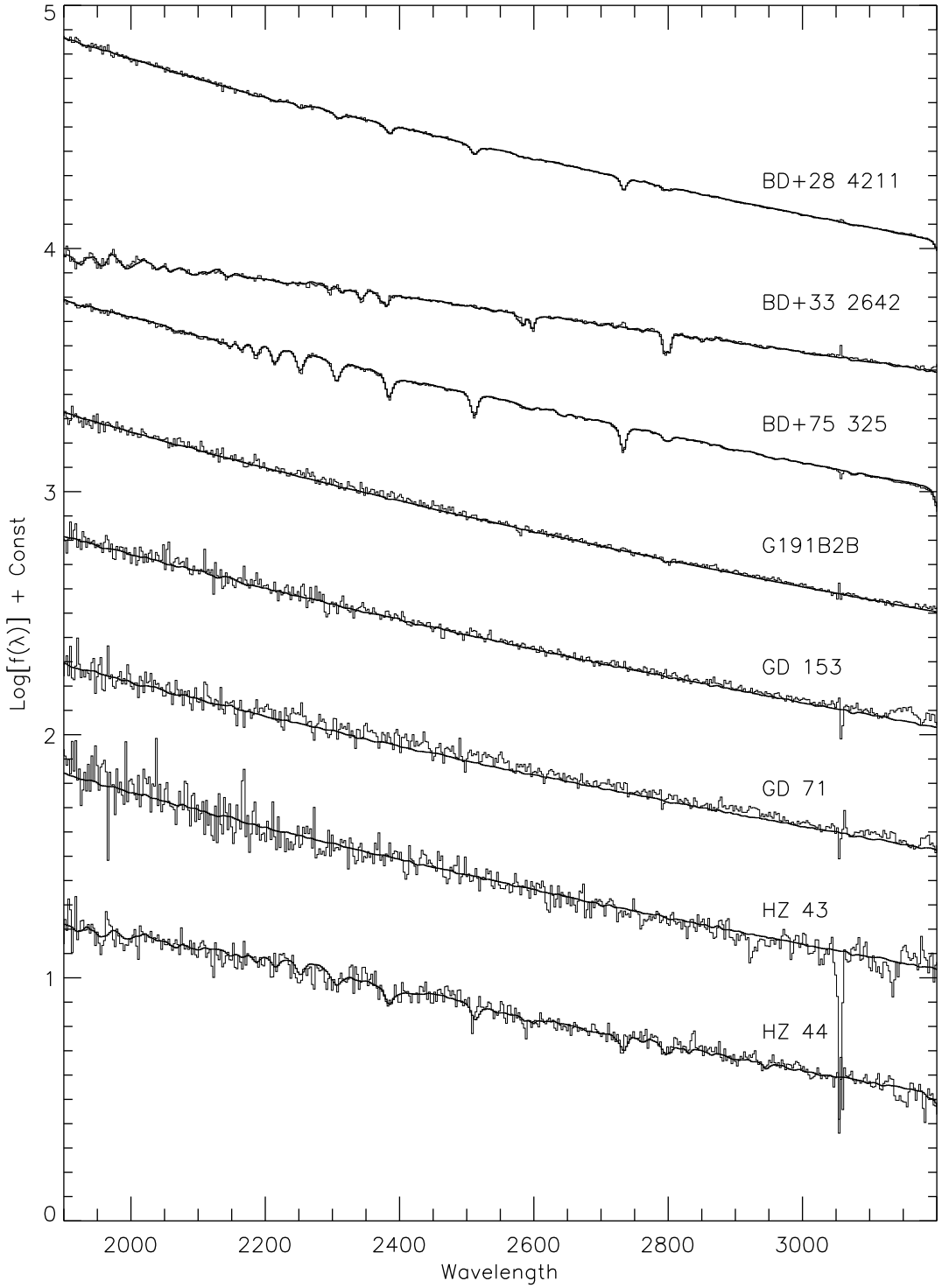

Fig. 9a.— Comparison of FOS data (thick curve) and fully corrected NEWSIPS LWP data (thin curve) for stars in common. The FOS data have been degraded to the *IUE* resolution.

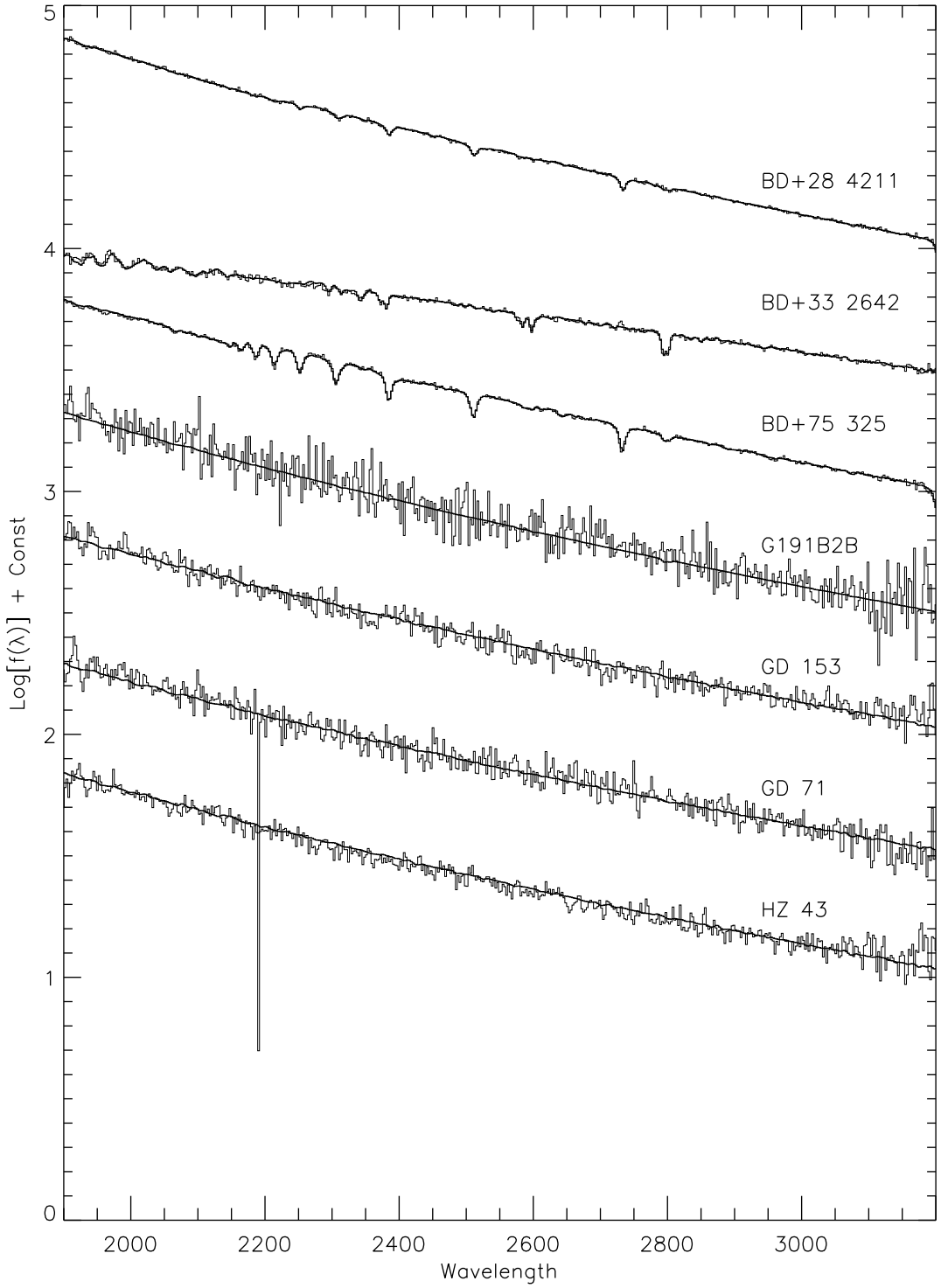

Fig. 9b.— Same as Figure 9a for the LWR data.

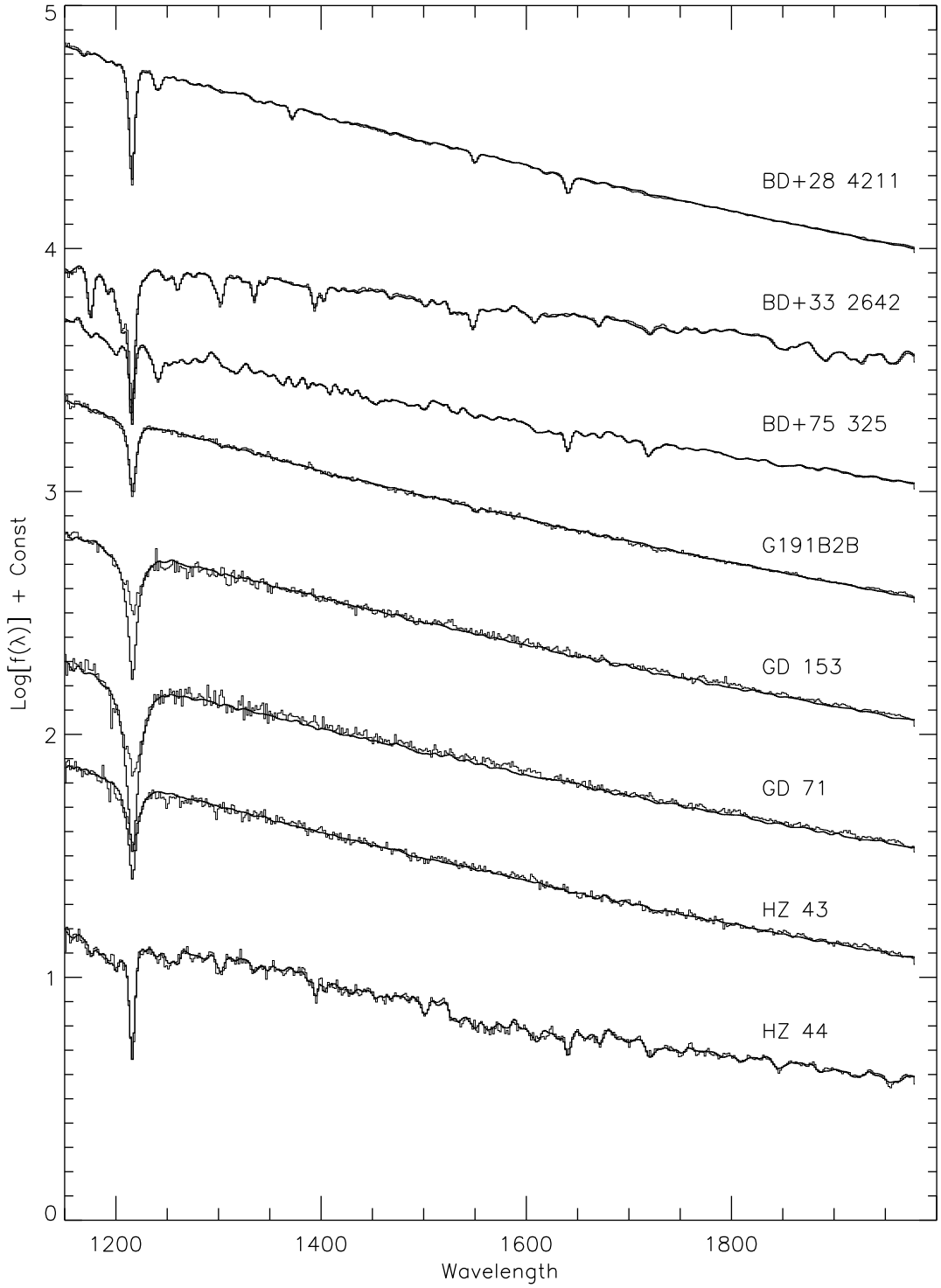

Fig. 9c.— Same as Figure 9a for the SWP data.

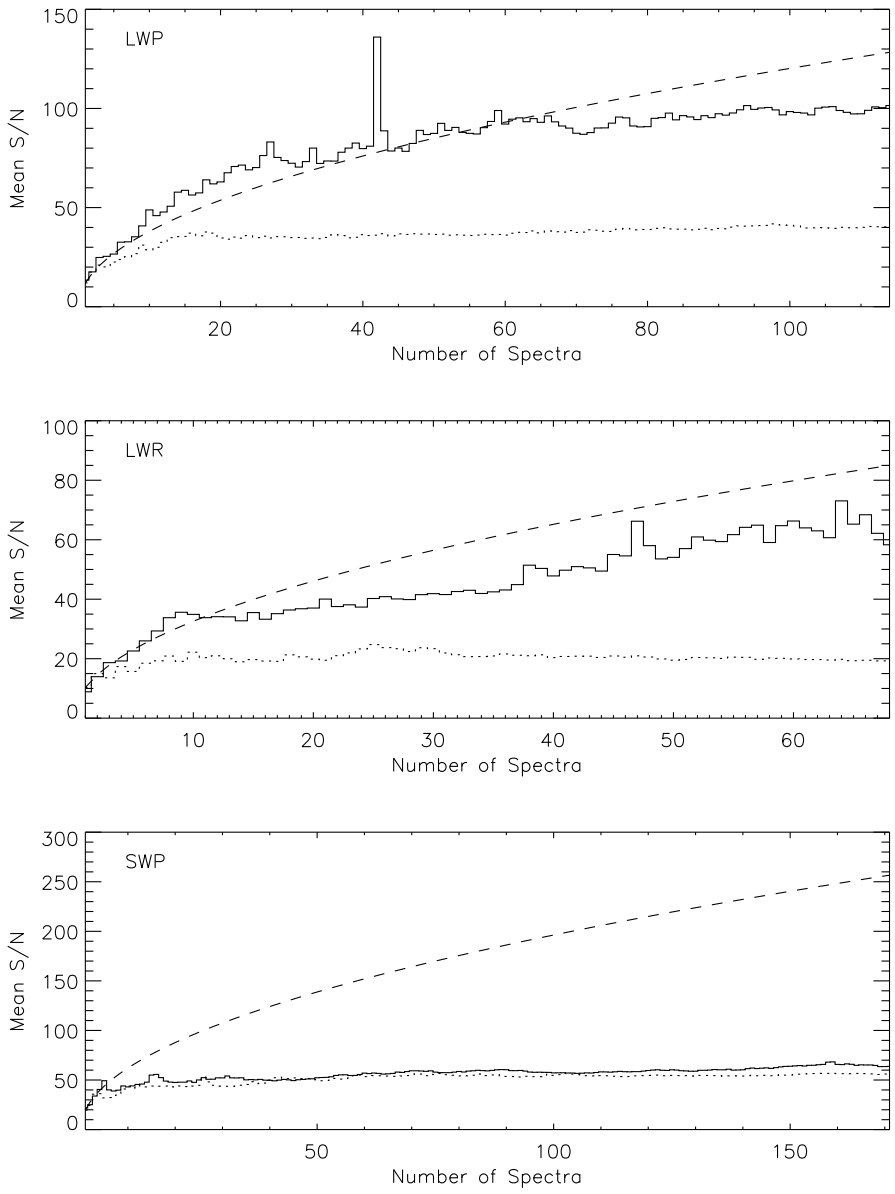

Fig. 10.— Comparison of S/N values (see §7) as a function of the number of spectra averaged to make the mean. Large aperture spectra of HD 93521 were used in the calculations. Results determined from NEWSIPS data are indicated as dotted curves, fully corrected NEWSIPS results are solid curves and the theoretical, systematic-free limits are dashed curves. The relevant camera is indicated in each plot.

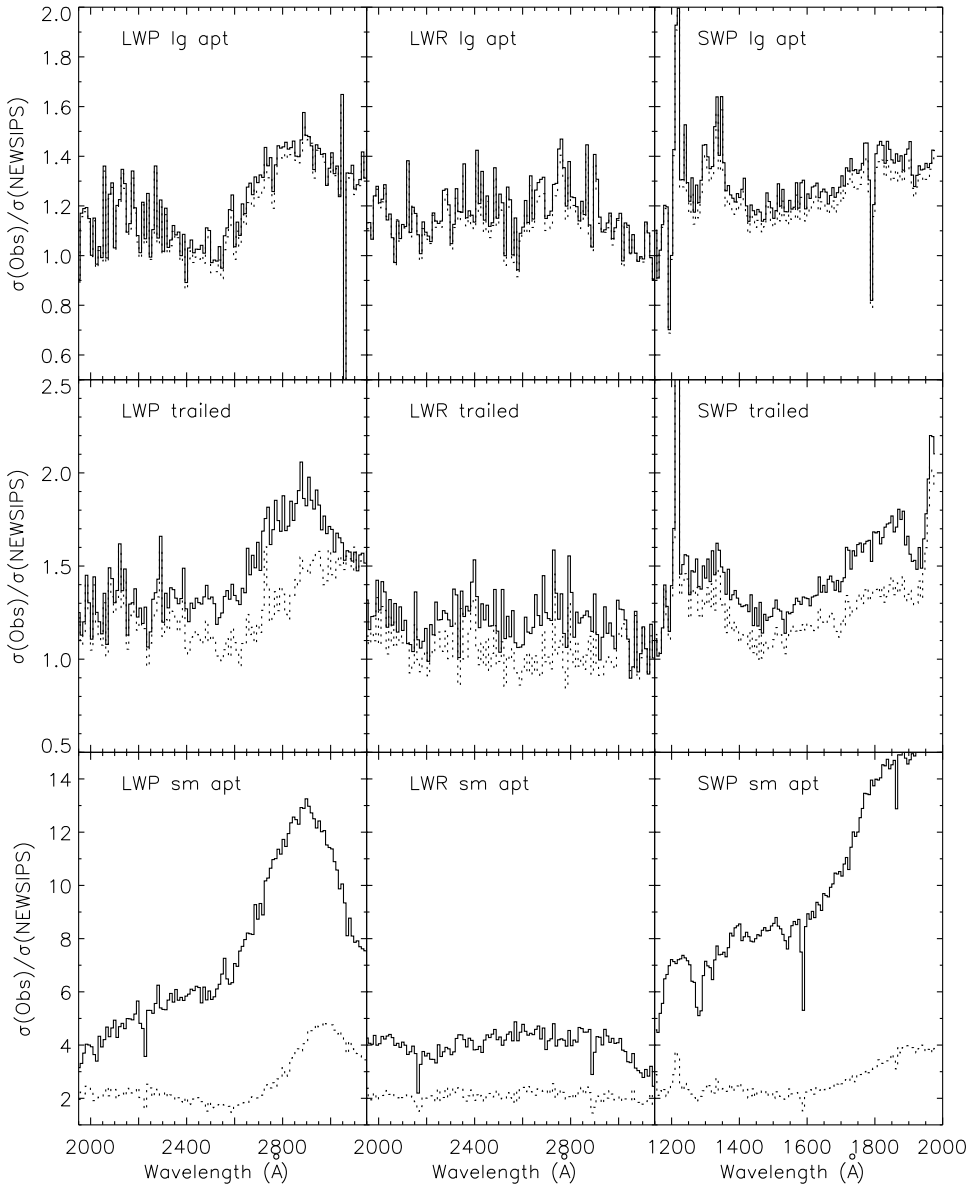

Fig. 11.— Ratio of the observed standard deviations, $\sigma(Obs)$, to errors derived from the NEWSIPS error models, $\sigma(NEWSIPS)$, for the mean of the 3 standard stars; HD 60753, BD+28°4211 and BD+75°375. There is one panel for each camera-observing mode combination, and there are 2 curves for each star. The solid curves are for $\sigma(Obs)$ derived from fully corrected, unscaled observations and the dotted curve is for $\sigma(Obs)$ derived from fully corrected spectra which have been rescaled to a common mean over a fixed wavelength band.

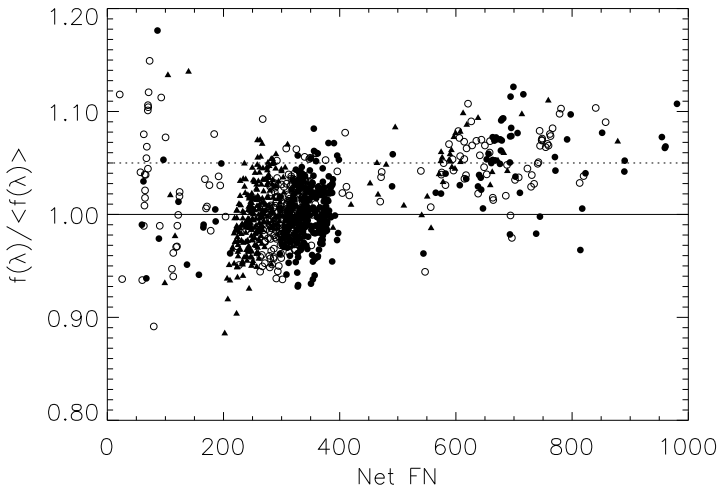

Fig. 12.— Exposure level systematics in BD+28°4211 (full circles), HD 60753 (triangles), and BD+75°375 (open circles). The plot shows mean NEWSIPS flux values over the wavelength region $2350 < \lambda < 2400$ Å for each star divided by the mean for all exposures with linearized flux numbers (*FN*) in the range $200 < FN < 400$. Fluxes derived from saturated pixels and pixels from an extrapolation of the ITF were not included. This figure demonstrates that LWP fluxes derived from exposures with large *FN* values are systematically larger than average, indicating a problem with the LWP ITF (see, §7.

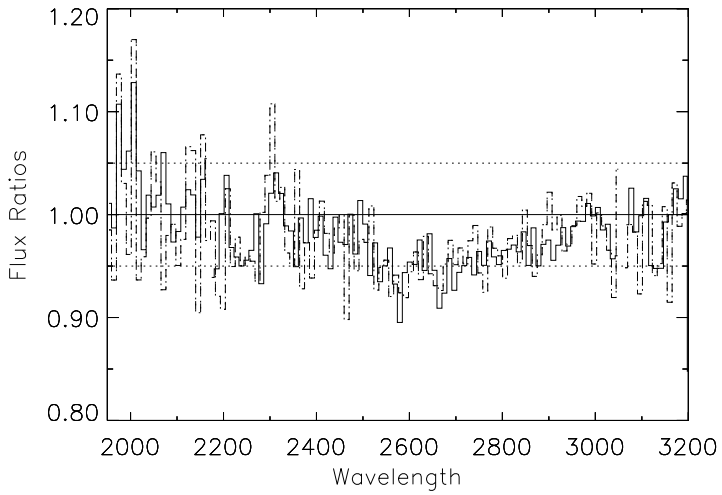

Fig. 13.— Ratios of long and short exposures for BD+28°4211 (full curve), HD 60753 (dotted), and BD+75°375 (dashed). The plot shows the ratio of mean NEWSIPS fluxes for spectra selected to have *FN* values in the range $200 < FN < 400$ over the wavelength band $2650 < \lambda < 2700$ Å divided by spectra selected to have *FN* values in the range $200 < FN < 400$ over the same band. Data from saturated pixels and pixels using an extrapolated ITF were excluded.